Lawrence Berkeley National Laboratory
Recent Work

Title
PION-MASS MEASUREMENT BYCRYSTAL DIFFRACTION OF MESONIC X RAYS

Permalink

Author
Shafer, Robert Eugene.

Publication Date
1965-12-22

University of California

Ernest O. Lawrence Radiation Laboratory

PION-MASS MEASUREMENT BY CRYSTAL DIFFRACTION
OF MESONIC X RAYS

Berkeley, California

DISCLAIMER

This document was prepared as an account of work sponsored by the United States Government. While this document is believed to contain correct information, neither the United States Government nor any agency thereof, nor the Regents of the University of California, nor any of their employees, makes any warranty, express or implied, or assumes any legal responsibility for the accuracy, completeness, or usefulness of any information, apparatus, product, or process disclosed, or represents that its use would not infringe privately owned rights. Reference herein to any specific commercial product, process, or service by its trade name, trademark, manufacturer, or otherwise, does not necessarily constitute or imply its endorsement, recommendation, or favoring by the United States Government or any agency thereof, or the Regents of the University of California. The views and opinions of authors expressed herein do not necessarily state or reflect those of the United States Government or any agency thereof or the Regents of the University of California.

UNIVERSITY OF CALIFORNIA

Lawrence Radiation Laboratory
Berkeley, California

AEC Contract No. W-7405-eng-48

PION-MASS MEASUREMENT BY CRYSTAL DIFFRACTION OF MESONIC X RAYS

Robert Eugene Shafer

Ph. D. Thesis

December 22, 1965

PION-MASS MEASUREMENT BY CRYSTAL DIFFRACTION OF MESONIC X RAYS

Table of Contents

PION-MASS MEASUREMENT BY CRYSTAL DIFFRACTION OF MESONIC X RAYS

Robert Eugene Shafer

Lawrence Radiation Laboratory
University of California
Berkeley, California

December 22, 1965

ABSTRACT

The design, operation, and calibration of the 7.7 meter bent crystal spectrometer, used for mesonic x-ray studies at the 184" Cyclotron are described. Using the spectrometer, the energies of the 4F-3D transitions in pionic calcium and titanium are measured and found to be 72.352 $\pm$ 0.009 keV and 87.651 $\pm$ 0.009 keV respectively. Theoretical calculations of the relationship between the transition energies and the charged pion mass are presented. Comparison of the calculations with the experimental measurements yields

$$M_\pi c^2 = 139.577 \pm 0.014 \text{ MeV}$$

as a new estimate of the charged pion mass.

The conservation of energy in the $\pi \rightarrow \mu + \nu$ decay process is examined by making use of other experimental results, and an upper limit of 2.1 MeV (68 per cent confidence level) is assigned to the mass of the muon neutrino.

I.   INTRODUCTION

Crystal diffraction spectrometry of pionic x-rays has been recognized for more than a decade, in principle at least, as being probably the most precise method of measuring the mass of the π^- meson. That such a measurement has not already been made reflects the fact that a) crystal spectrometers are inefficient, and b) the pion beam intensities available from existing accelerators are inherently low. In this paper, a bent crystal spectrometer is used to compare the wavelengths of two pionic x-rays to the wavelength of a nuclear γ ray. The experiment yields an estimate of 139.577 ± 0.014 MeV for the π^- mass.

In the course of studies with cosmic rays and artificial sources, the pion mass has been measured many times with varying degrees of precision. These experiments are reviewed by several authors.[1-4] It is instructive, however, to briefly review several of these measurements in order to indicate the methods used and the range of precision obtainable.

Observation of the discontinuity of the attenuation coefficient of pionic x-rays near the K absorption edge of selected filters allowed Stearns et al.[5] to place upper and lower limits on the π^- mass. Specifically the 4F-3D transitions of pionic phosphorus, aluminum, and potassium were observed to lie above the energy of the Ce K edge, below the Sb K edge, and below the Hf K edge, respectively. As the energies of the absorption edges are measurable by crystal spectrometers, they are accurately known, and hence place precise limits on the energies of the pionic x-rays. Once the relationship between the π^- mass and the transition energies is understood, it is possible to place limits on the π^- mass. The three transitions mentioned above limit the π^- mass

to the interval 139.15 ± 0.15 MeV $\leqslant M_\pi c^2 \leqslant 139.76 \pm 0.20$ MeV.

The Q value of the absorption process $\pi^- + p \rightarrow n + \gamma$ is directly related to the π^- mass, since the process takes place at rest. The two-body final state yields a 130 MeV γ-ray and an 8.8 MeV neutron, each of which bears a unique energy relationship with the π^- mass.

Crowe and Phillips[6] in 1954 used a focusing pair spectrometer with an energy resolution of 1.7 MeV (fwhm)[7] to measure the γ-ray energy. The measured energy of the γ-ray, 129.19 ± 0.18 MeV, yielded a π^- mass estimate of 139.37 ± 0.20 MeV.

The Q value of this absorption process can also be obtained by application of time-of-flight techniques to the neutron. Using a 50 foot (differential) flight path and an effective time resolution of 14 nsec (fwhm), Czirr[8] measured the neutron flight time to be 372.2 ± 1 nsec, which yields a π^- mass estimate of 139.69 ± 0.41 MeV. Some consideration has been given to a possible new measurement of the neutron velocity, and it is believed that with a longer flight path (~ 300 feet) the experiment could yield a measurement of the π^- mass with about ± 0.02 MeV[9] precision.

The development of the mass-ratio technique in nuclear emulsions over a period of several years resulted in the measurement of the π^+ mass by Barkas, Birnbaum, and Smith[10] in 1956. As the rate of energy loss for charged particles is dependent only on their velocity, the residual ranges of two similarly charged particles with the same initial velocity will be in the ratio of their respective masses. In this experiment, velocity selection was made on the pions and protons by utilizing the Cyclotron magnetic field. 60 proton and 368 π^+ tracks were examined, yielding (using the present proton mass) 139.68 ± 0.15 MeV for the mass of the π^+.

A byproduct of this mass-ratio experiment was the measurement of the absolute muon momentum in the decay $\pi^+ \to \mu^+ + \nu$. Two separate measurements, comprising a total of 364 decays, yielded a combined value of 33.94 ± 0.05 MeV for the $\pi^+ - \mu^+$ mass difference, under the assumption that the uncharged particle has zero mass. Combining this mass difference with the present value of the muon mass (105.659 ± 0.002 MeV)[11] yields a π^+ mass of 139.60 ± 0.05 MeV. This represents the presently accepted value.

The error on the best pion mass estimate at present contributes significantly to the error on the mass estimates of several heavier particles, most notably the charged kaons. Equally significant is the fact that the best values of all the meson masses are based on the accepted value of the charged pion mass, which is based in turn on a single series of emulsion experiments. A precise independent measurement of the pion mass is therefore desirable.

As the measurement presented here is of the π^- mass, a check of the energy conservation in the process $\pi^+ \to \mu^+ + \nu$ is possible. Upper limits can be placed on either the muon neutrino mass or the $\pi^+ - \pi^-$ mass difference, assuming the other to be zero.

Using the above technique, Barkas et al.[10] have placed an upper limit of 3.6 MeV on the muon neutrino mass. Two other experiments have been able to place upper limits on the muon neutrino mass by energy conservation in μ decay. Dudziak et al.[12] report an upper limit of 4.1 MeV, and Bardon et al.[13] an upper limit of 2.6 MeV.

As a $\pi^+ - \pi^-$ mass difference would violate CPT invariance,[14] the exact equivalence of the π^+ and π^- mass will be assumed a priori.

II. THE BENT CRYSTAL SPECTROMETER

A. General Considerations

The optimum energy region for bent crystal spectrometry of x and γ rays is the interval 20 keV $\leqslant$ E $\leqslant$ 200 keV, where the obtainable precision approaches the fundamental limit of $\pm$ 15 ppm, due to the energy-wave-length conversion constant $V\lambda$ = 12,372.42 $\pm$ 0.19 xu-keV.[15]

As will be seen in Section III, a precise relationship between the pion mass and pionic x-ray energies is at present only known for low energies, E $\lesssim$ 100 keV, where the effects of the π-nuclear interaction are small. Hence the bent crystal spectrometer is an excellent instrument for measuring the π mass by the pionic x-ray technique.

The principle of exact focusing of curved crystals was conceived by DuMond and Kirkpatrick[16] in 1930, and construction of the first bent crystal spectrometer suitable for precision γ-ray spectroscopy was completed in 1947.[17] Since then many similar instruments have been built, and several review articles have been written[18-22] covering the design and operation of these spectrometers, including a comparison of the various geometries suitable for bent crystal diffraction. In particular, DuMond's article[19] and Knowles' article[22] should both be referred to for their discussions of the aberrations in bent crystal spectrometers.

In the application of crystal diffraction spectrometry to mesonic x-ray studies, special consideration must be given to the proper design of the spectrometer. The mesonic x-ray "source" intensities available with existing accelerators are in the micro-Curie range, as opposed to the Curie-sized radioactive sources usually associated with crystal spectrometers. Furthermore, pion beams and mesonic x-ray "sources" are

not as flexible as radioactive sources in their adaptability. In brief, the crystal spectrometer should be designed to complement the mesonic x-ray "source", and not vice versa.

The crystal spectrometer design chosen for the mesonic x-ray studies at the 184" Cyclotron is the DuMond geometry with a long (7.7 m) focal length. It should be realized that each type of crystal spectrometer (i.e. DuMond, Cauchois, single flat, and double flat) offer certain advantages, and that with the development of more intense pion beams and better experimental techniques, one of the alternate geometries may eventually be preferable.

A detailed discussion of the design, operation, and calibration of the spectrometer is presented in the next two sections. Those readers who are not particularly interested in this aspect of the experiment are asked to proceed directly to Part III.

B. Mechanical Description of Spectrometer

As is common practice in bent crystal design, this instrument consists of three physically separate units: 1) the source; 2) the crystal pivot assembly; and 3) the collimator-detector assembly. The mechanical construction of the latter two is discussed in this section. One of the design requirements is that the source be at a stationary focus of the spectrometer. Therefore both the crystal and the collimator-detector assembly are rotatable.

This instrument bears a close resemblance to other instruments already constructed. Overall it is quite similar to the Argonne 7.7 meter spectrometer,[23] except for the Bragg-angle measuring system, which is more closely comparable to the new Cal. Tech. 2 meter instrument.[24] Figure 1 illustrates the optical geometry of the instrument described
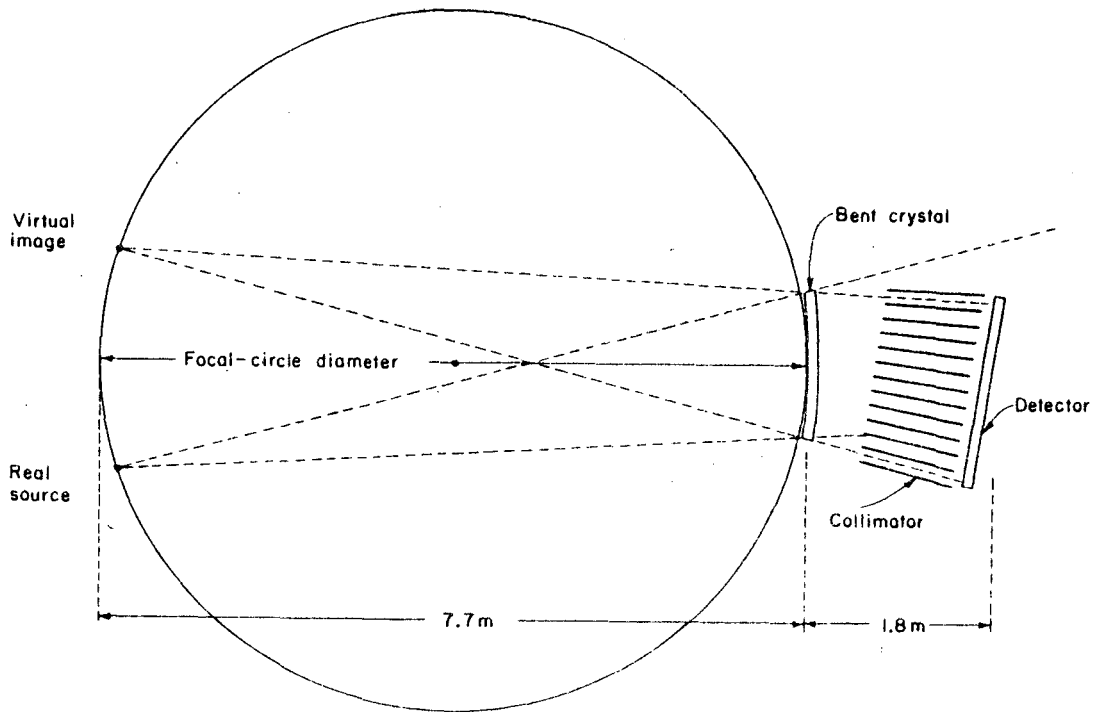
Fig. 1: Optical geometry of the 7.7 m bent crystal spectrometer. When
the Bragg conditions are satisfied, radiation from the source is
partially diffracted by the bent crystal, forming a virtual image.
The collimator is oriented to selectively transmit radiation from
the virtual image.

here, and Table I summarizes some of the more important parameters.

Overall top and side views of the spectrometer are illustrated in Figures 2 and 3 (the radiation shielding is not shown in these illustrations and will be discussed later). The foundation is a 30 ton concrete block on a shock-absorbent mounting. A surplus Navy gun mount is used to support and rotate the entire detector-collimator assembly (including about 5 tons of shielding), and a counterweight to balance the assembly. As moments about the gun mount are approximately can-celled, rotation of this assembly is not expected to affect the align-ment of the spectrometer.

Mounted rigidly to the concrete foundation through a hole in the center of the gun mount is the crystal pivot assembly. This assembly is illustrated in Figure 4. Ball bearings were used here since their load carrying capability is greater than slide bearings, and they could be supplied with the necessary precision. The central bearings are special class 9 Fafnir ball bearings with a maximum radial runout of 50 μ inches and ball sphericity within 5 μ inches. The two bearings are preloaded against each other with 1000 pounds force to remove all axial and radial play. The final machining of the crystal pivot table was done using these bearings to define the axis of rotation, hence minimizing table runout. The axial thrust is carried by the outer race of the lower bearing.

Above the bearings in Figure 4 is the 23 inch diameter engraved horizontal circle[25] used for positioning the collimator assembly with respect to the crystal orientation. Microscopes mounted on the gun mount are used to interpolate between the 0.1 degree inscriptions to a precision of ± 10 seconds (the collimator resolution (fwhm) is about
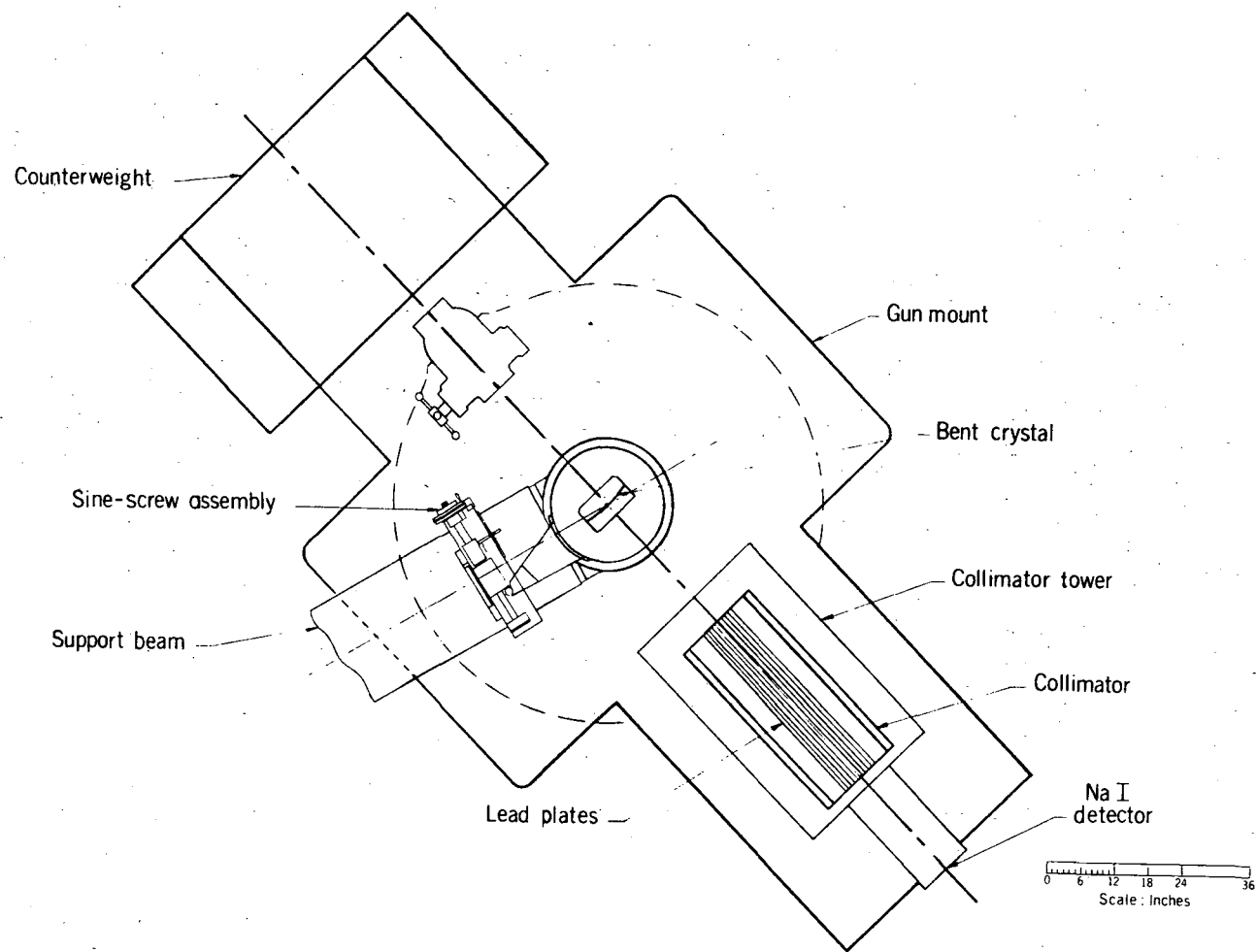
Table I.   Important Parameters of the Bent Crystal Spectrometer

Crystal:	Type	quartz (310)
	Dimensions	$20 \times 20 \times 0.6$ cm^3
	Aperture	160 cm^2
	Focal Circle Diameter	764 cm
	Intrinsic Resolution[a] (fwhm)	17 sec of arc
	Corresponding Energy Resolution (fwhm)[b]	$\Delta E = 1.6 \times 10^{-5}$ E^2 keV
	Projected Resolution at Target (fwhm)	0.063 cm
	Depth of Field	8 cm
	Maximum Overall Efficiency	$\sim 2.5 \times 10^{-6}$ at 50 keV
Sine Screw:	Maximum Measurable Angle[a]	27,000 sec each side of center
	Corresponding Minimum Energy[c]	40 keV
	Precision Presently Obtainable[a]	± 0.4 sec
	Corresponding Energy Precision[b]	$\sigma = \pm 3.8 \times 10^{-7}$ E^2 keV
Collimator:	Overall Dimensions	$18 \times 18 \times 94$ cm
	Plates	44 Pb alloy plates 1 mm thick
	Gaps	3 mm (tapered)
	Resolution (fwhm)	900 sec of arc
Detector:	Type	NaI (Tℓ)
	Dimensions	$17 \times 17 \times 0.63$ cm^3
	P.M. Tubes	9 RCA 6810's

[a] 1 sec $\cong$ 0.011 xu

[b] At 50 keV, the resolution is 40 eV (fwhm) and the obtainable precision about $\pm$ 1 eV.

[c] First order both sides

Counterweight

Gun mount

Bent crystal

Sine-screw assembly

Collimator tower

Support beam

Collimator

Na I detector

Lead plates

0 6 12 18 24 36
Scale : Inches

MU-36737
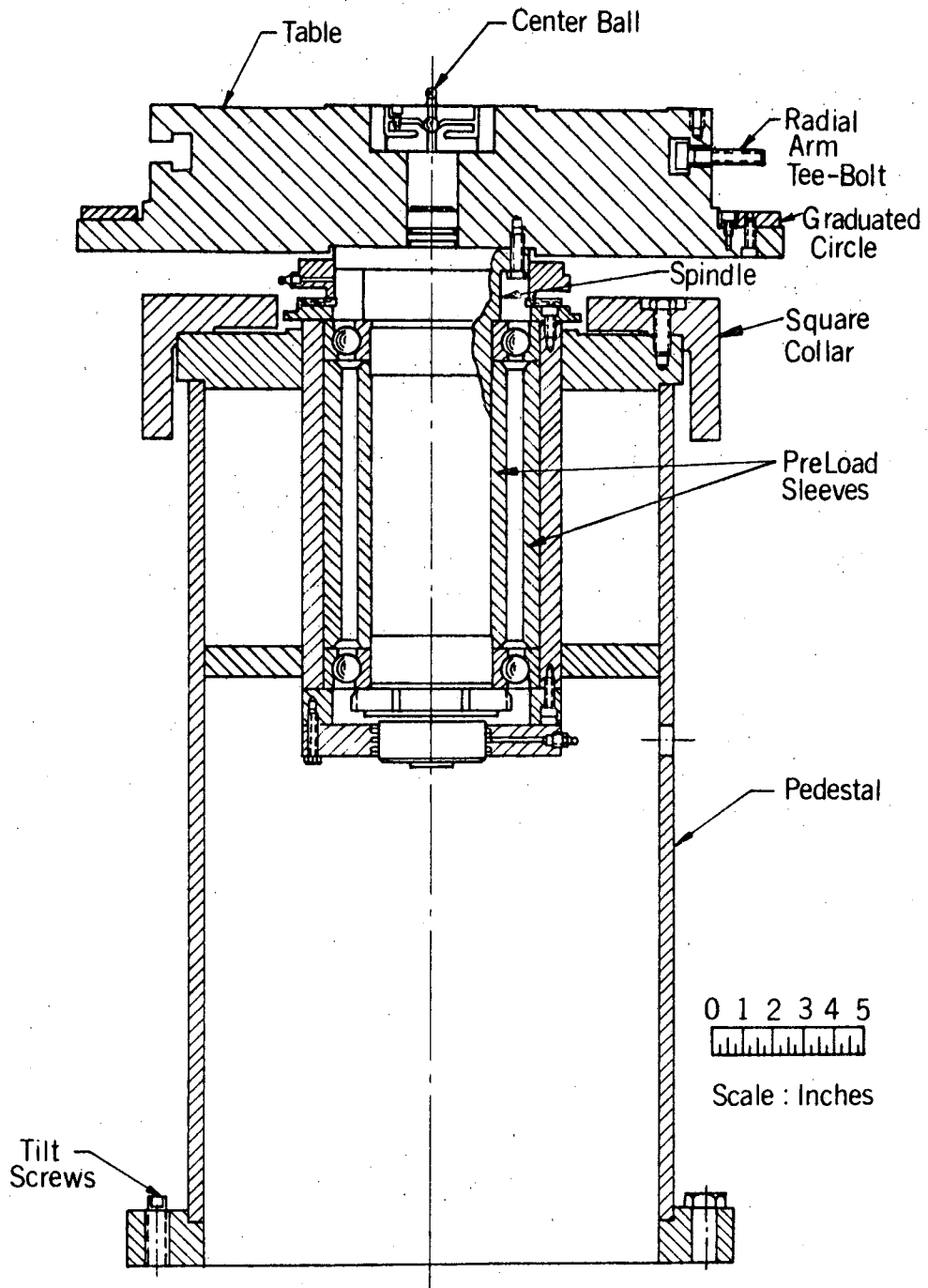
Fig. 2: Top overall view of the spectrometer. Radiation shielding around
the detector is not shown.
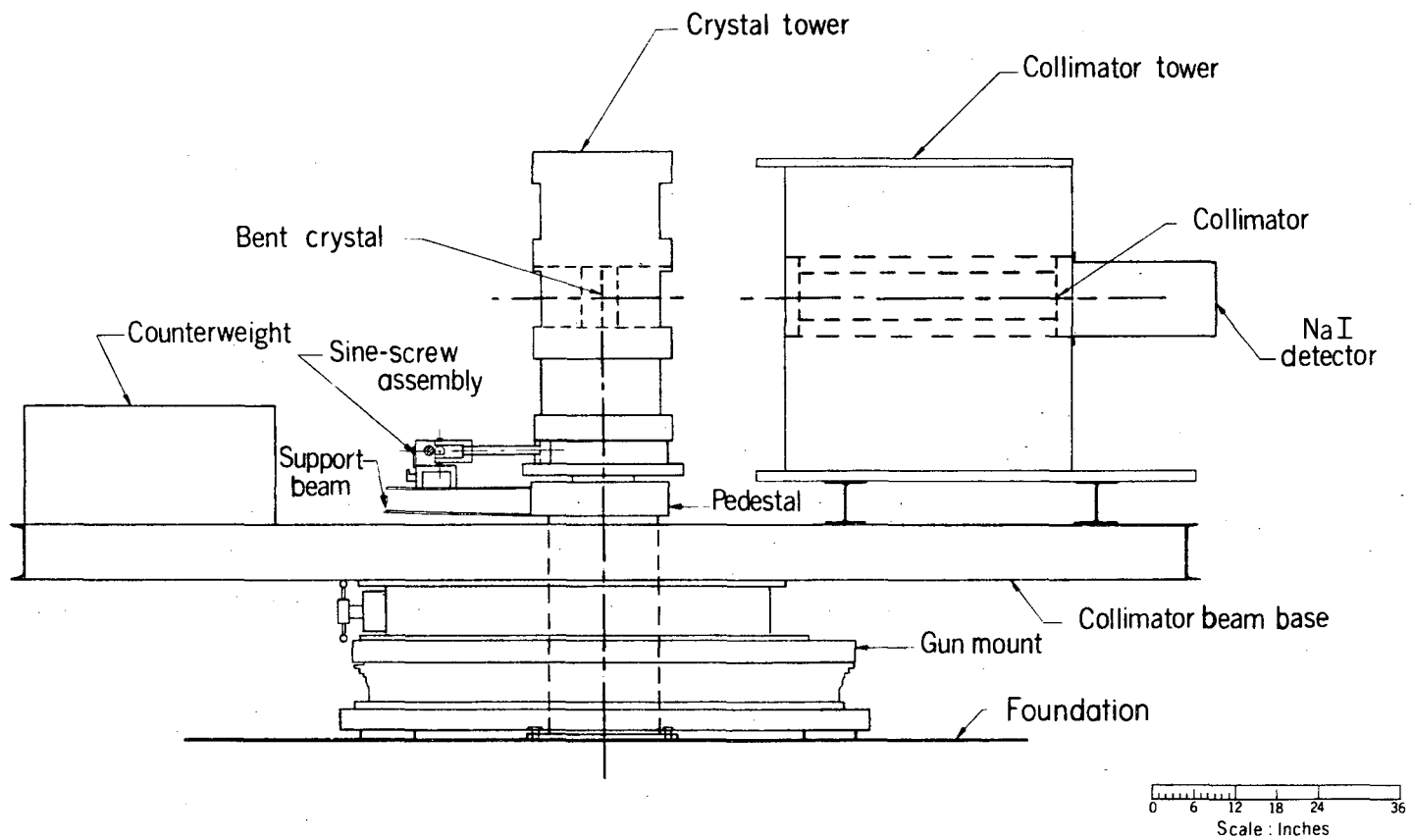
MU-36736

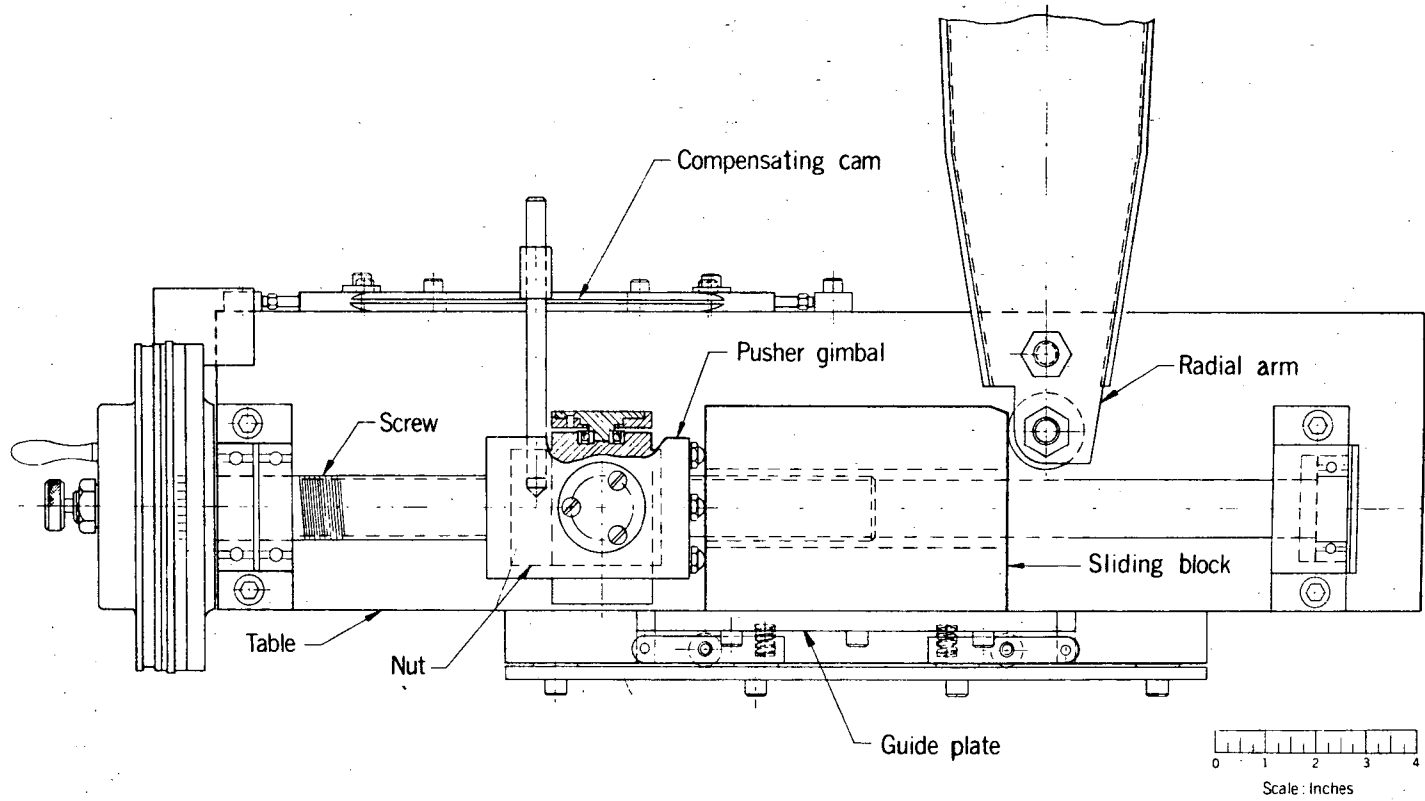Fig. 3: Side view of the spectrometer. Radiation shielding around the detector is not shown.

Fig. 4: The crystal pivot assembly. The bent crystal, when in place, is about 20 inches above the center ball.

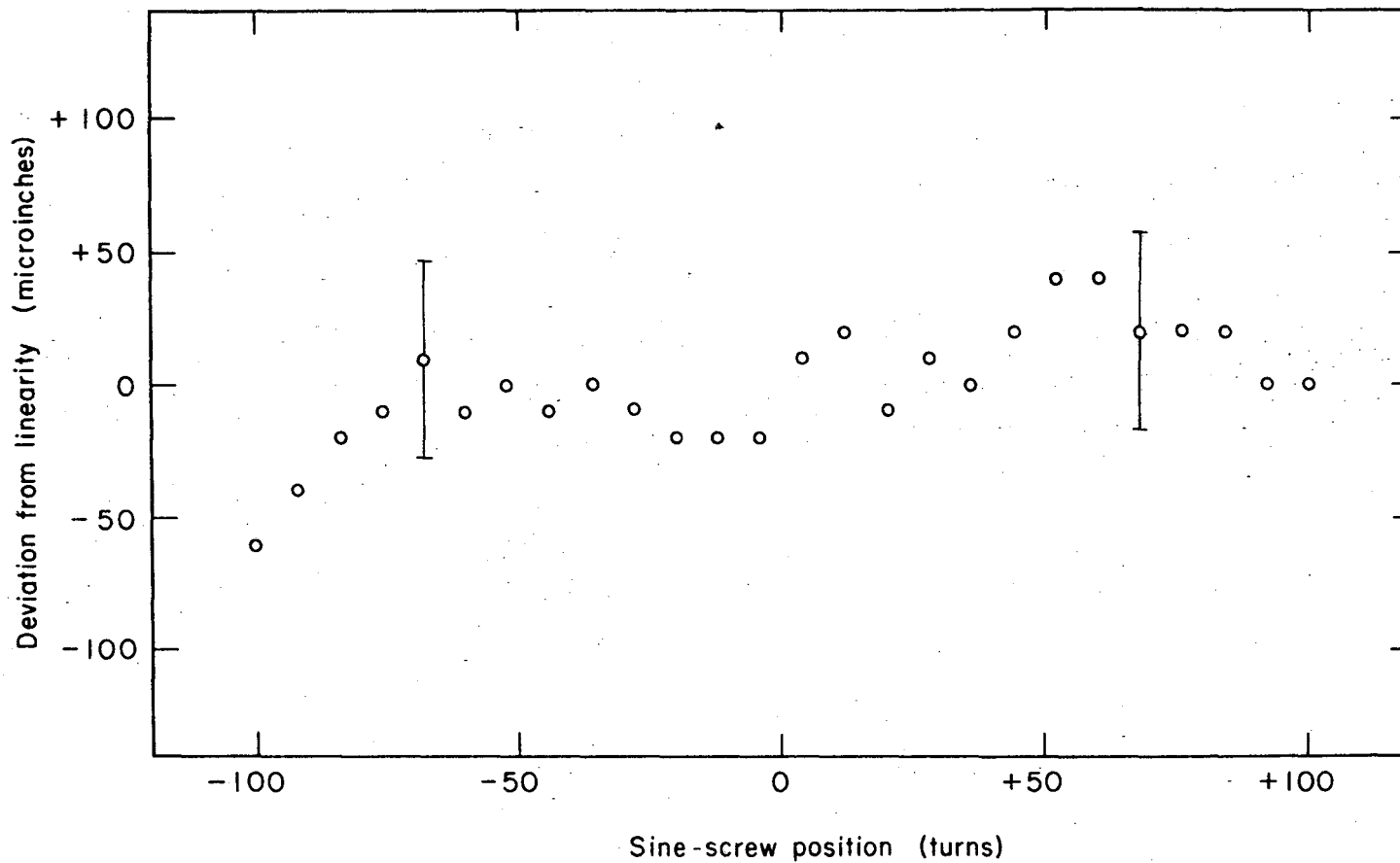900 seconds). The inscriptions are accurate within ± 1 second.

The sine-screw mechanism is illustrated in Figure 5. The 1.25 inch diameter stress-proof-steel lead screw is supported by class 9 Fafnir ball bearings, the axial thrust being borne by the two angular-contact preloaded bearings at the crank end. The bronze split-nut is attached to a full-gimbal yoke which makes a 3 point contact with the sliding block. The motion of the sliding block is collimated by a guide plate. The endplate of the sliding block pushes against a 1.5 inch diameter precision steel ball mounted in the pivot arm. A constant azimuthal torque is applied directly to the pivot arm by suspended-weight arrangement, the torque being counter-balanced by an axial thrust in the sine screw. The entire mechanism is enclosed in a dustproof lucite case.

The lead screw and the split nut were lapped together after the machining process, and a linearity check was made by comparison with a precision-engraved steel rule. The mean pitch was determined to be 32.0019 turns per inch, the deviations from linearity were found to be less than ± 37 μ inches, as illustrated in Figure 6. This is about the limit of precision obtainable by comparison with an engraved rule. A correction cam is provided for correcting non-linearities, but the precision required for mesonic x-ray measurements has not yet warranted its use (the error on the angular separation of the two Bragg peaks of the Ti 4F-3D transition discussed in a later section corresponds to a lead screw error of ± 220 μ inches). Synchronous axial motion of the lead screw, due to axial runout in the preloaded bearings, was determined to be 30 ± 5 μ inches peak-to-peak, using air gage techniques (as all the above linearity measurements were taken an integral number of turns apart, they are not correlated with the axial motion). Although

Compensating cam

Pusher gimbal

Radial arm

Screw

Sliding block

Table

Nut

Guide plate

Scale: Inches

0 1 2 3 4

MU-36739

Fig. 5: The sine-screw mechanism.

Fig. 6: Linearity check of the lead screw. The data are the average of three runs. The error flag represents the assigned linearity, being ± 37 μ inches, corresponding to ± 0.004 xu for first-order diffraction from quartz (310).

the axial motion can be corrected for in the data analysis, it is negligible as far as the mesonic x-ray measurements are concerned. The length of the pivot arm is 22.0000 ± 0.0002 inches, and the useable region of the lead screw is about 90 turns each side of center, allowing measurement of Bragg angles up to 27,000 seconds each side (this corresponds to a lower limit of 40 Kev first-order both-sides for quartz (310) diffraction). The total mechanical error, including both systematic (non-linearity) and statistical (non-repeatability) contributions, is expected to be within ± 46 μ inches, which corresponds to ± 0.43 seconds of arc (these errors correspond to ± 0.005 xu for diffraction from quartz (310) planes).

The crystal clamp blocks (the method of imprisonment is used here) were cast from type 420 stainless steel, annealed, and then ground on a machine specifically built for this application.[26] Both the convex and concave form blocks were then lapped against cast iron blocks ground to the same radius of curvature. The convex form block has an aperture of 13.7 x 13.7 cm^2 with a single 1.6 cm wide rib across the center, leaving about 160 cm^2 open area.

The quartz plate, supplied by Hilger and Watts Ltd. to the same specifications as required by Argonne,[23] was cut to 20 x 20 x 0.6 cm^3 with the (310) planes normal to the two faces and two edges. The plate, etched with HF to reduce the possibility of breakage, was clamped between the form blocks with a 0.2 cm thick neoprene gasket on the convex side. Observation of "Newtons rings" type interference between the steel rib and the quartz plate indicated the contact to be within a micron everywhere. Figure 7 illustrates the imprisoned crystal.

With the increased knowledge of crystal growing techniques,
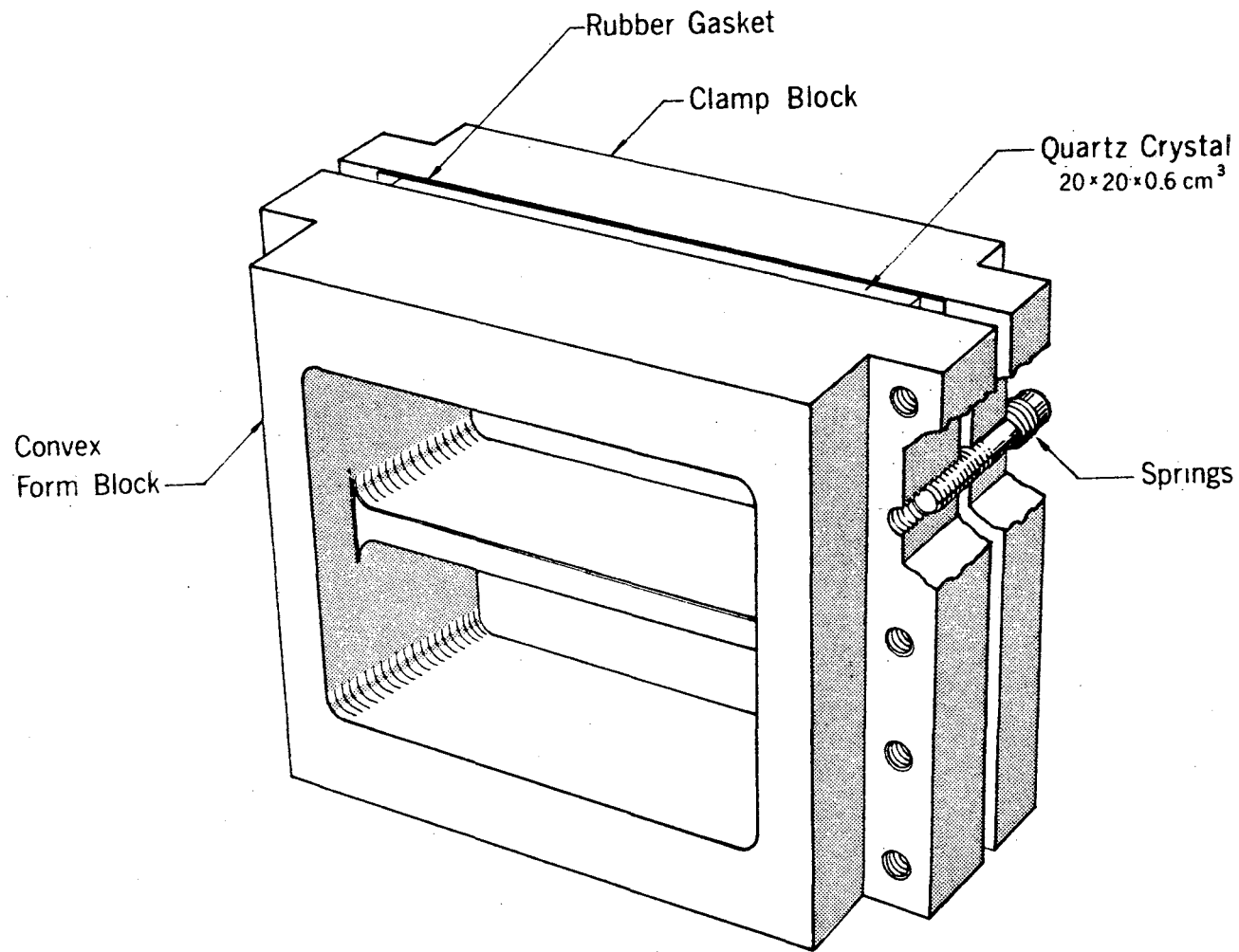
MU.36719

Fig. 7: The crystal clamp blocks with the crystal in place. The radius of curvature is 7.7 meters. The optical alignment target, mounted on the convex block during the pionic x-ray experiment, is not illustrated.

however, and the development of intense mesonic x-ray sources, diffraction

planes other than quartz (310) should certainly be considered. For

high precision work the trend should be toward smaller d spacings like

quartz (502) or multiple-order diffraction from germanium (400) and

(422). Large d spacings, like quartz (101), sacrifice resolution for

higher reflectivity, and therefore should be reserved for "discovery",

as opposed to "precision", measurement.

A cross-section of the collimator is shown in Figure 8. It is

of the flat plate, tapered gap design, the plates being 1 mm thick and

the gaps approximately 3 mm wide. The 44 Pb alloy plates were manufact-

ured from low-background lead supplied by the St. Joseph Mines. The

collimator has an aperture of about 18 x 18 cm^2 and is 94 cm long.

Construction included stretching the plates lengthwise, fastening them

to the upper and lower guide plates with a room-temperature-cure epoxy,

and finally stretching them vertically as indicated in the Figure. The

collimator, designed for use at low energies (Bragg angles > 1°), has

an estimated transmission effeciency of 0.65, based on the performance

of an earlier design. The measured resolution is about 900 seconds of

arc for 84 keV γ-rays.

The detector is a 17 x 17 x 0.63 cm^3 packaged NaI(Tℓ) viewed

on one face by 9 RCA 6810's through a 2" long lucite light pipe. The

system was balanced for uniform pulse-height output over the entire NaI(Tℓ)

surface by using a radioactive source and varying the anode voltages

individually. The choice of NaI(Tℓ) as the scintillator depended both

on pulse height resolution and timing resolution and will be discussed

in a later section.

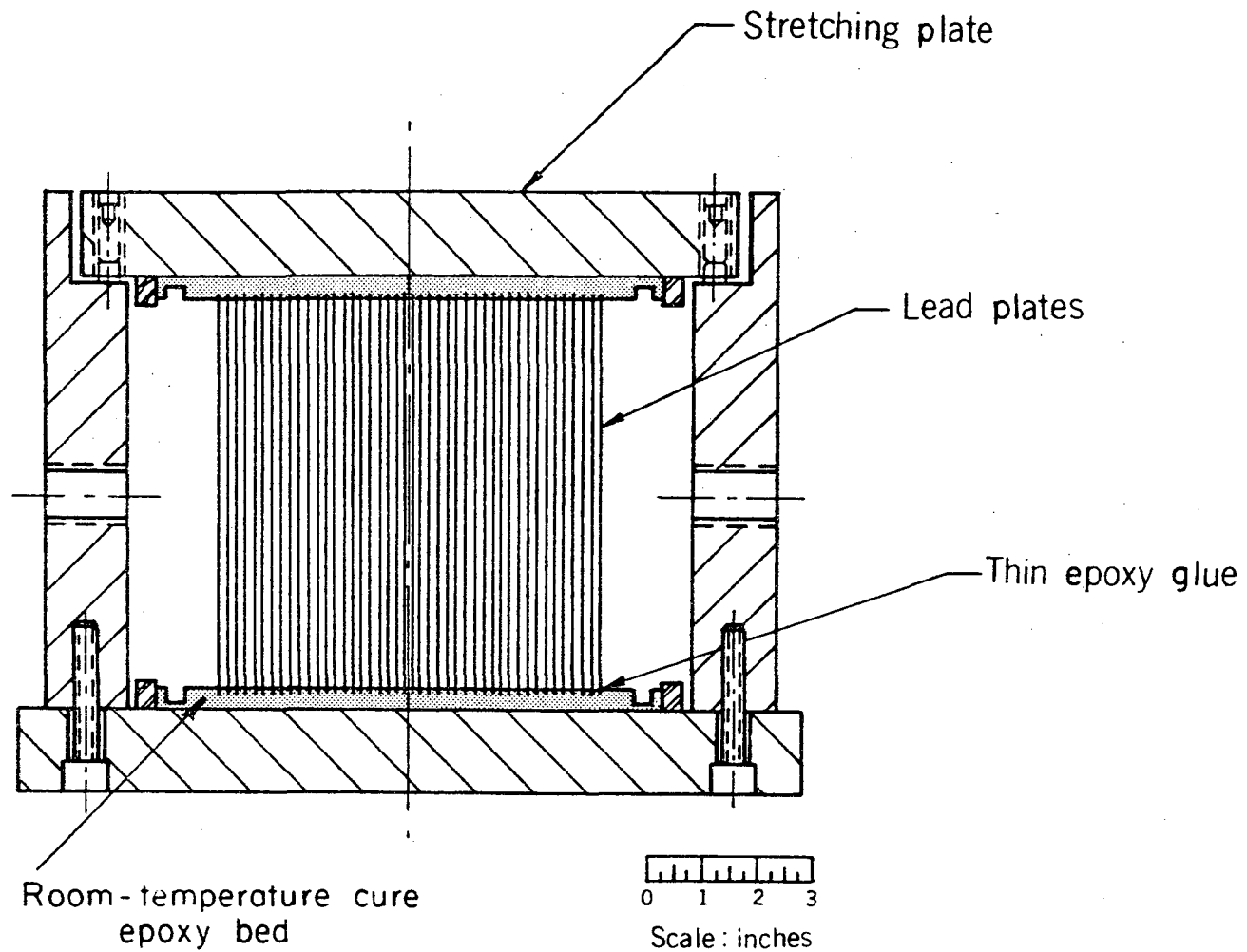Due to the high neutron background existing around the 184"

Fig. 8: The bent crystal collimator. The Pb alloy plates are stretched in two dimensions during installation to insure flatness.

MU-36738

Cyclotron, the shielding required around the NaI detector and collimator is quite extensive. The entire system is (almost completely) surrounded by a minimum of four inches of lead. Outside the lead is a combination of paraffin and boric acid, the average thickness being about twelve inches. Inside the lead is one layer of Bor-Al plate[27] to capture thermal neutrons (Boron is perferable to cadimum because of the low capture-gamma yield. Also the Bor-Al plate, being non-hydrogenous, will not thermalize fast neutrons, but allow them to escape the enclosure, hopefully to be thermalized outside the lead). The total weight of this shielding is about 5 tons, and is counter-balanced as shown in Figures 2 and 3.

In addition to this shielding, the bent crystal "cave" is surrounded (on five sides) by a combination of concrete (minimum thickness about four feet) and battleship iron (minimum thickness one foot). None of the weight of this additional shielding rests on the foundation of the bent crystal.

The result of all this shielding is that the background level of the NaI detector is about 0.09 counts/keV-sec in the region 50 to 100 keV (with some energy dependence). Turning the Cyclotron beam on and off produces less than a 5 per cent effect, indicating the background to be due mainly to natural radioactivity in the construction material of the NaI detector, collimator, collimator tower, and shielding. The effect of cosmic rays and tube noise is small.

Many bent crystal spectrometers have automated systems for rotating the crystal and collimator assemblies while simultaneously maintaining the proper relative alignment. In this spectrometer, however, both assemblies are manually moved, the relative alignment

being checked with a microscope. As the pionic x-ray events rate is
of the order of two counts per hour, the automated equipment was not
considered necessary.

C. Performance and Calibration

The quality of the bent crystal was checked by performing a
Hartmann test[28] with a 0.5 Curie Au^{198} source. The 0.25 mm diam gold
wire, irradiated at the Livermore-Pool-Type Reactor, was held taut and
vertical by a 500 g weight. The test indicated that the focusing
properties were quite uniform, even near the edges, and hence that the
entire aperture could be used. The optimum focal circle diameter was
determined to be about 764 cm, 6 cm shorter than expected (the first
crystal installed in the 7.7 m Argonne spectrometer showed a similar
deviation).

Diffraction from the entire crystal yielded an optimum resolution
of 17 sec of arc (fwhm) as shown in Figure 9. As this corresponds to
an effective source width of 0.63 mm, the contribution from the finite
diameter of the gold wire is small: Least squares analysis of the
diffraction peak shows that it is reasonably symmetric and may adequately
be represented by a Gaussian distribution. (It is important to note
that any instrumental asymmetry will occur in both the right and left
diffraction peaks with the same parity, so that when the Bragg angle
is found by measuring their angular separation, any effect of the
asymmetry will be completely cancelled.)

The energy resolution (fwhm) is then (keV units):

$$\Delta E = 1.6 \times 10^{-5} E^2 \tag{1}$$

for first-order diffraction. The mechanical errors mentioned in Section
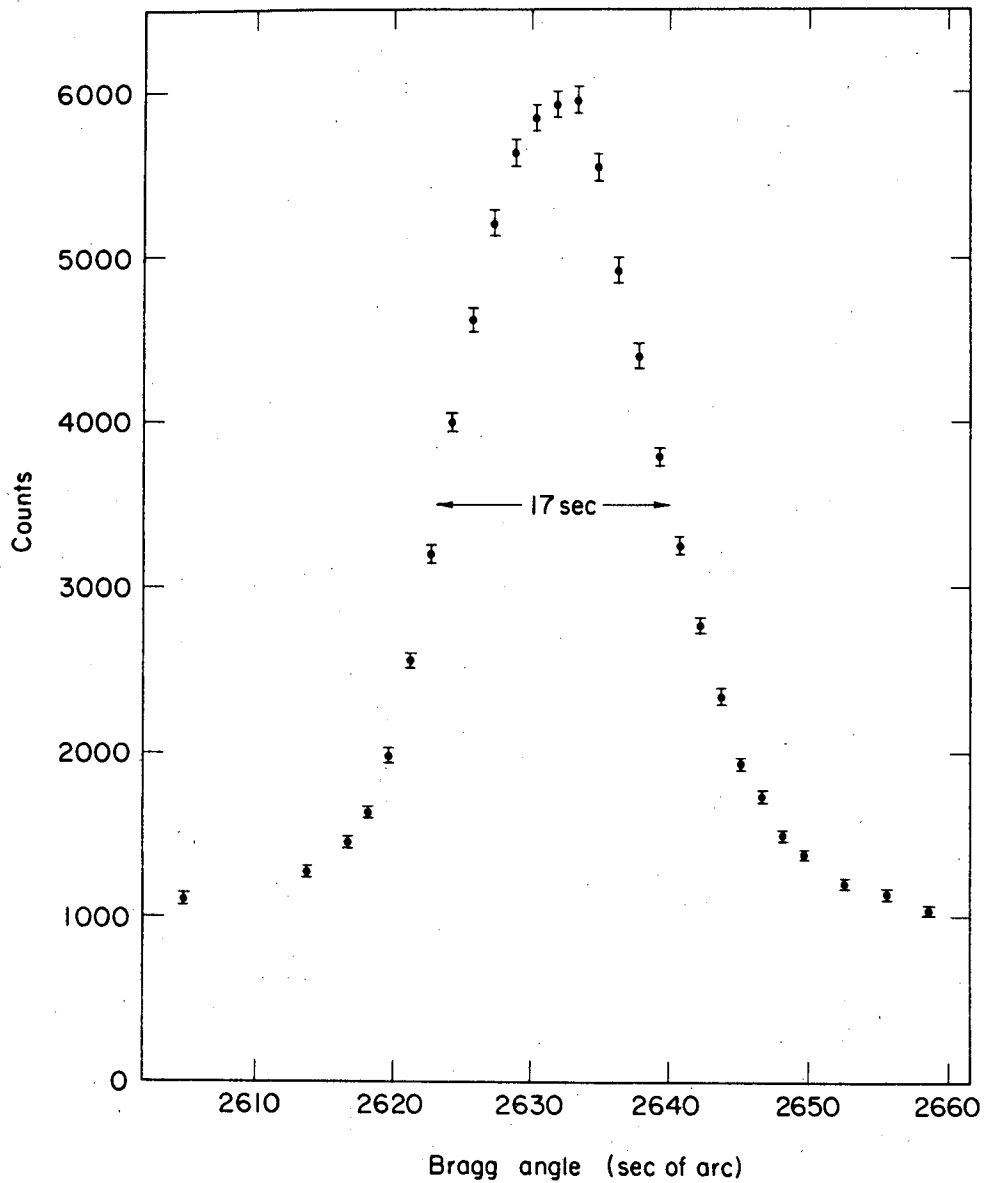
MU-36765

Fig. 9: First-order Bragg diffraction peak for a 0.25 mm diameter
Au[198] source. Optimum resolution is 17 sec of arc (fwhm).

IIB presently limit the precision to about 2.5 per cent of the resolution (note that by convention, resolution is measured in fwhm, and precision in standard deviations).

The total efficiency may be calculated from geometrical factors, absorption coefficients of air and quartz, and the crystal reflectivity. The mechanical solid angle subtended by the crystal is $4\pi \times 2.2 \times 10^{-5}$ steradians, and the estimated transmission efficiency of the collimator is 0.65.

When x-rays are transmitted through a crystal in such a way that the Bragg conditions are satisfied, a fraction of the total transmitted intensity, defined here as the reflectivity, is expected to be in the diffracted beam. The integrated reflectivity is the reflectivity integrated over the diffraction peak. Secondary extinction refers to the removal of intensity from either the incident or diffracted beams by (multiple) diffraction in the crystal (i.e., the maximum reflectivity is 0.5). This apparent saturation of the reflectivity can affect the shape of the diffraction peak. Primary extinction, a coherent process taking place in the small "perfect" mosaic "blocks" within the macroscopic crystal, has been shown by Lind et al.[29] to be negligible in bent quartz crystals for the wavelength region of interest here, and will not be discussed further. The reflectivity of the quartz crystal used here is expected to exhibit the $1/E^2$ energy dependence of mosaic crystals, modified only by the secondary extinction process. The interested reader is referred to Lind et al.[29] and Zachariasen[30] for a more complete discussion of the diffraction process in perfect and mosaic crystals.

The reflectivity of the 6 mm thick bent quartz crystal may be

derived from the integrated reflectivity measured for a 1 mm thick bent quartz crystal by Lind et al.[29] The calculated reflectivity is illustrated in Figure 10. The effect of secondary extinction is observable below 100 keV. The total efficiency, based on reflectivity, absorption, and geometrical factors, is shown in Figure 11. As can be seen, below 50 keV the efficiency drops off rapidly due to absorption of the x-rays in air and the quartz crystal. The maximum efficiency is expected to be about 2.5×10^{-6} at an energy of 50 keV.

The remainder of the performance tests, and the final calibration, were carried out with a 1 mm diameter, 10 cm high Tm^{170} source, in a quartz tube. The 0.5 Curie source was in the form Tm_2O_3. The radiations of interest are the nuclear gamma ray and the $K\alpha_1$ x-ray of Yb^{170}:

Transition	Wavelength	Energy
84 keV γ ray	146.835 ± 0.005 xu	84.261 ± 0.003 keV[31]
$K\alpha_1$ x-ray	236.165 ± 0.003 xu[15]	52.389 ± 0.001 keV

The wavelength-energy conversion constant used throughout this paper is 12372.42 xu-keV ± 15 ppm.[15] It is worthwhile to mention that the spectrometer resolution for the x-ray, which has a natural width of 35 eV, is 45 eV; hence the observed lineshape is distinctly different for the two radiations, the x-ray showing the "skirt" typical of resonances.

The most precise method of measuring Bragg angles is to measure the angular separation of the right and left diffraction peaks, in this case first-order. It is of considerable importance to check the repeatability of the instrument in order to understand as well as possible the sources of error.

The sine-screw mechanism measures the sine of the angle between
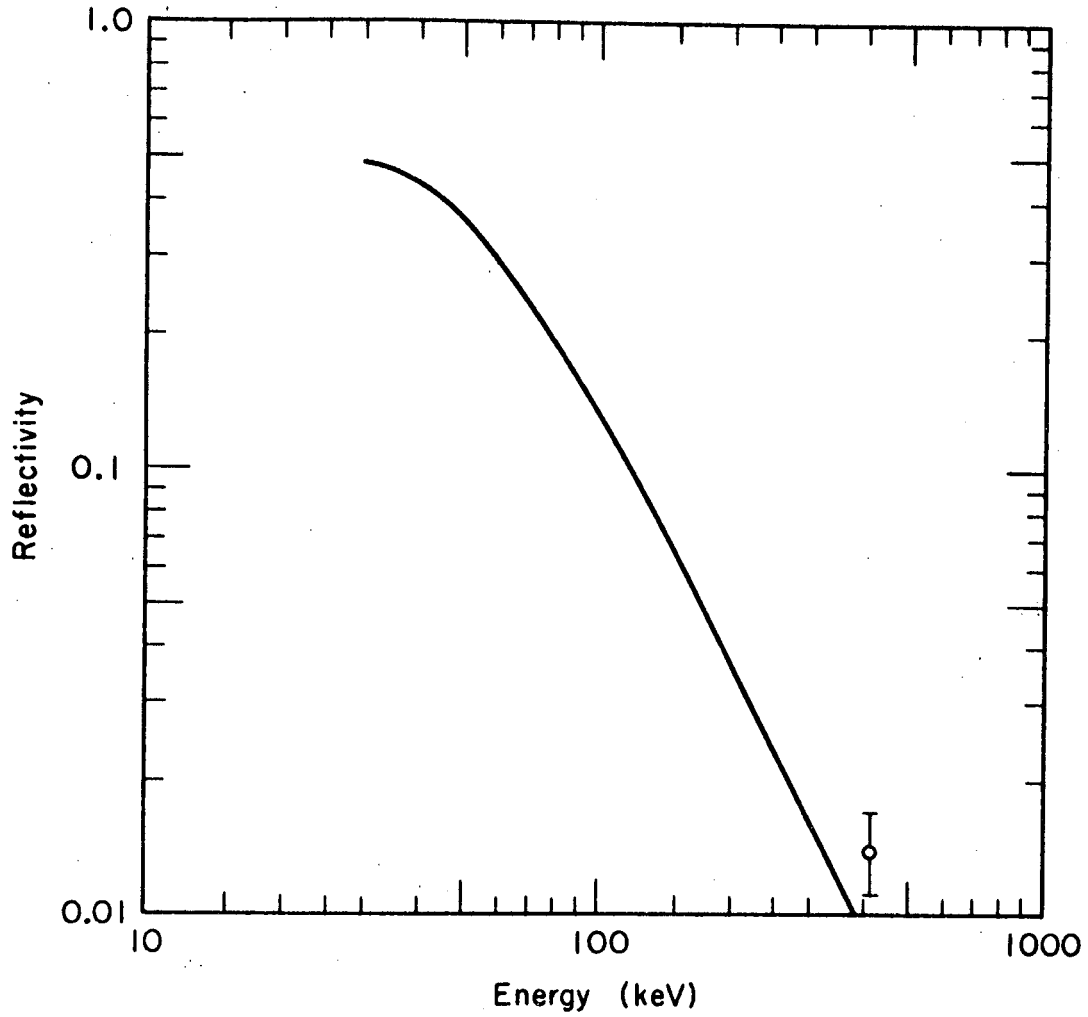
MU-36767

Fig. 10: The calculated reflectivity of a 6 mm quartz (310) crystal. Note the effect of secondary extinction below 100 keV. The point at 412 keV is measured with an Au[198] source.
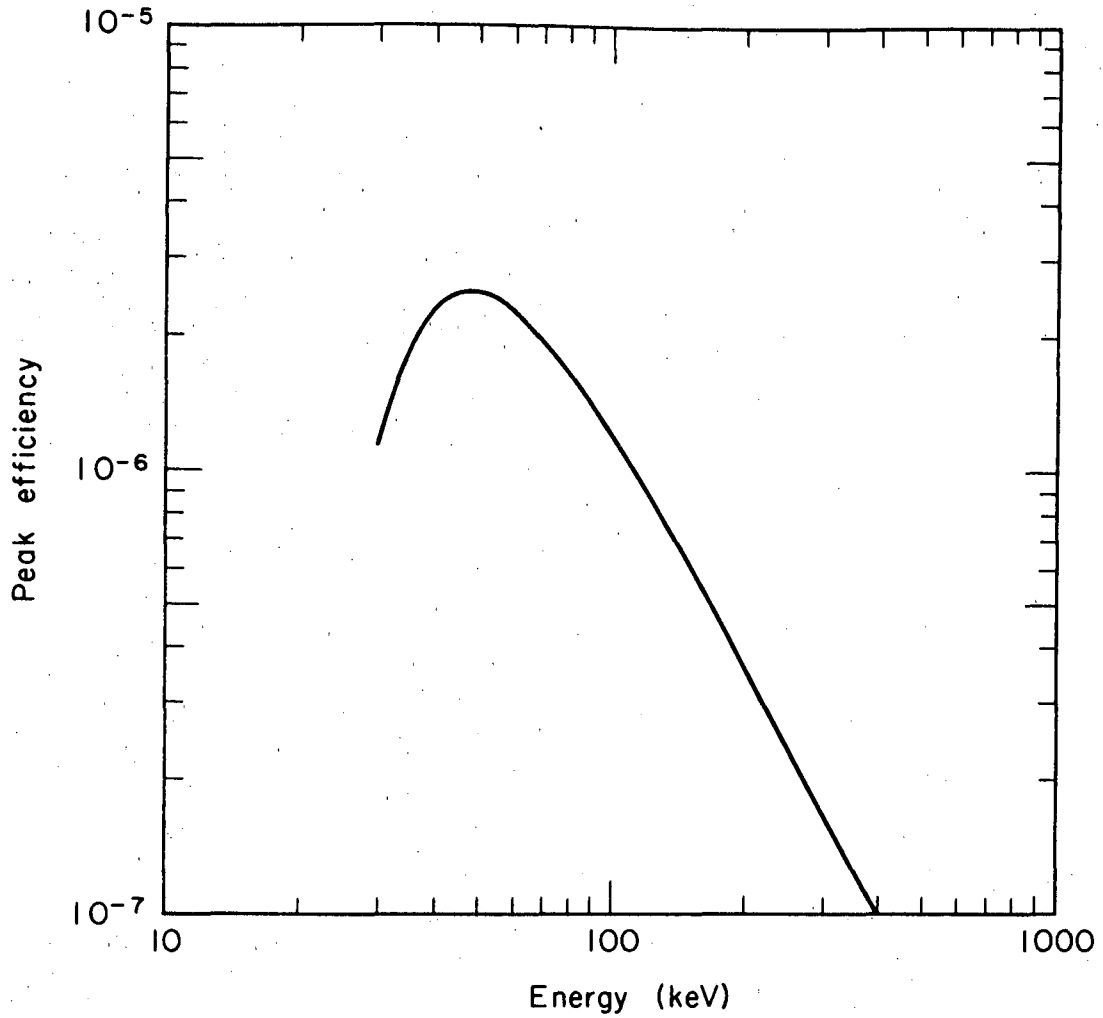
MU-36766

Fig. 11: Calculated total efficiency for the 0.6 x 20 x 20 cm^3 quartz
crystal when used with the present collimator. This does not include the
effects of finite source width, natural linewidth, or detector
efficiency.

the diffraction peak and a point on the lead screw defined mechanically to be the "mechanical center". As the angular separation between the right and left first-order diffraction peaks is $2\Theta_B$, the sine screw mechanism measures $2 \sin \Theta_B \cos \delta$, as shown in Figure 12. The angle δ is variable from approximately -1° to $+1^\circ$ by moving the source. Figure 13 shows measured values of $\sin \Theta_B \cos \delta$, using the 84 keV γ ray, plotted vs the midpoint (which is defined in Figure 12.).The smooth curve is a best fit of the form $A \cos \delta$, the expected shape.

The thermal expansion coefficient of the quartz (310) planes is 15 ppm per degree C.[32] The only other thermal expansion correction, due to differential expansion of mechanical parts, is believed to be less than ± 5 ppm effective contribution per degree C. No such anomalous temperature dependence has been observed. By convention, all measurements are corrected to 18°C.

Long-term stability is important. In Figure 13, seven of the points were measured before the pionic x-ray experiment, and three afterward. The observed shift is less than 10 ppm.

The error flags in Figure 13, determined purely on the basis of external consistency (i.e., from residuals), represent a deviation of ± 15 ppm, corresponding to a wavelength precision of ± 0.002 xu (about ± 0.2 Fermi). In each case the sample mean of the diffraction peaks were determined by χ^2 analysis, and the purely statistical fluctuations was estimated (see Equation A-6) to be less than ± 5 ppm. Although the wavelength precision is ± 0.002 xu and hence somewhat smaller than the ± 0.005 xu predicted by mechanical considerations, it should be realized that this test only compares the relative linearity of two regions of the sine-screw, each about 30 turns wide.

The location on the sine-screw of all the (pairs of) diffraction
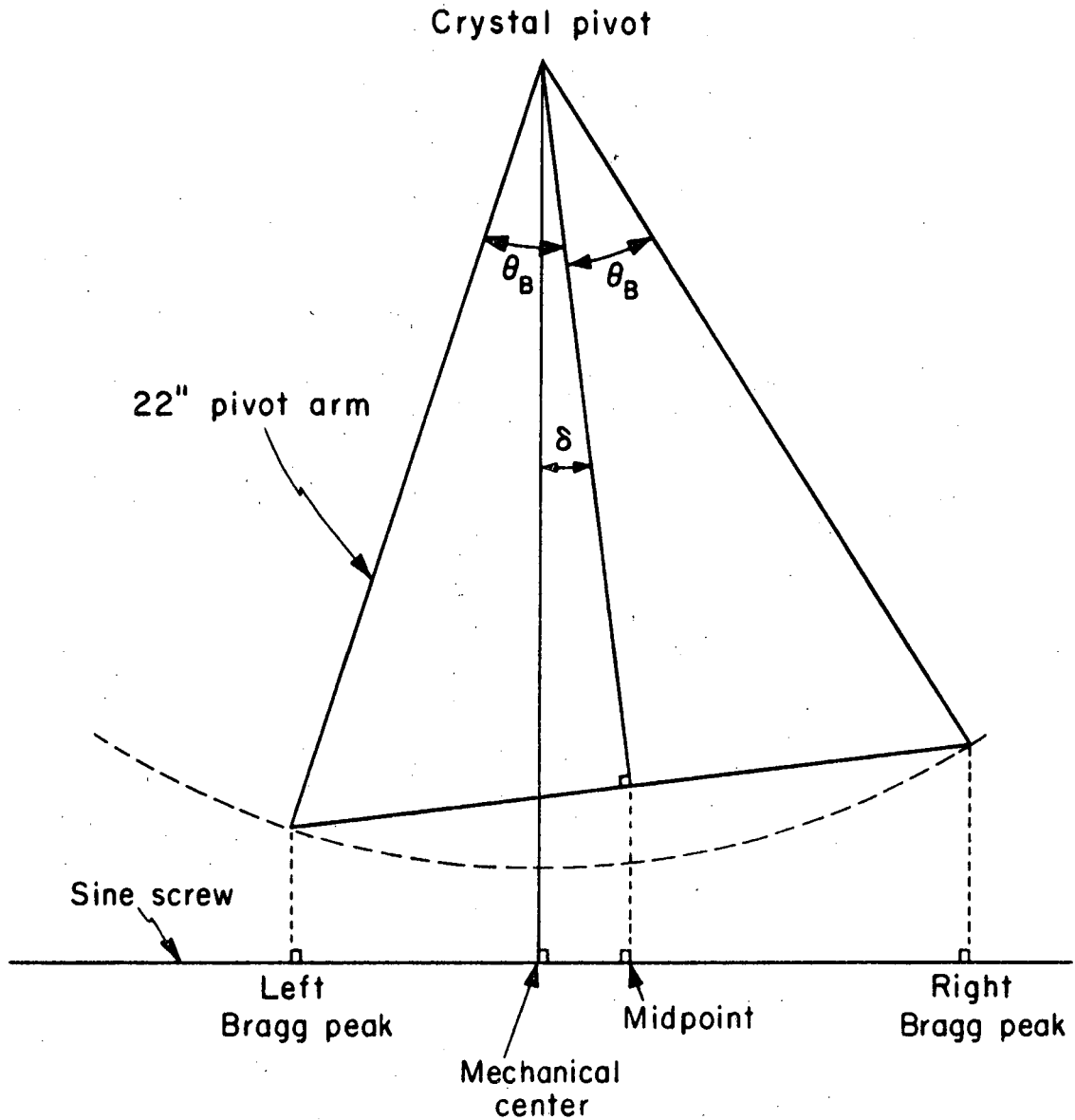
Fig. 12: Schematic representation of the operation of the sine-screw mechanism. The positions of the Bragg diffraction peaks and the midpoint are measured in units of sine-screw turns from the mechanical center.
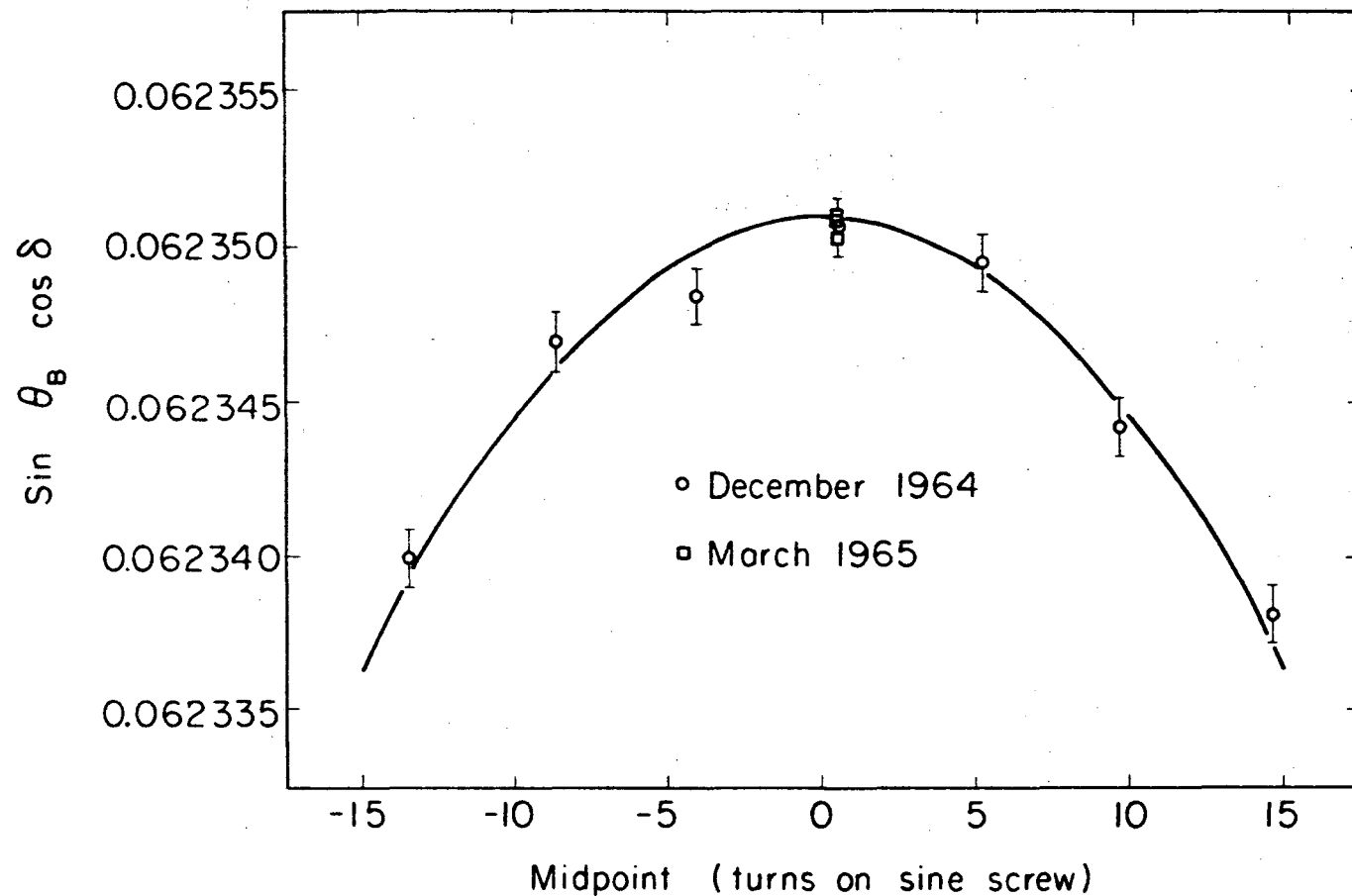
MU.36804

Fig. 13: Plot of sin θ_B cos δ vs midpoint (see Figure 12 for definition of terms) for diffraction of the 84 keV Yb^{170} γ-ray. The error flags represent a fractional error of $\pm$ 15 ppm, corresponding to a wavelength uncertainty of $\pm$ 0.002 xu. The pionic x-ray experiment took place between the two calibration dates.

peaks used in the calibration (including the electronic x-ray) are shown in Figure 14. Also shown is the placement of the two pairs of pionic x-ray diffraction peaks, whose measurement is described later. Note that all four pionic peaks fall within the two 30 turn wide regions.

The possibility that small-angle Compton scattering of x-rays in a thick source could produce a noticeable effect on the position or shape of the diffraction peak was considered. To test this, one inch of aluminum was placed directly in front of the source. No effect (other than attenuation) was observed within the limits of precision of the instrument.

The calibration of the instrument using the nuclear gamma and the electronic x-ray yielded the following data:

Transition	$\sin \Theta_B$	d_{18} Spacing
84 keV γ-ray	0.0623509	1177.49 ± 0.06 xu
52 keV x-ray	0.1002770	1177.56 ± 0.03 xu

The entire calibration error for each transition is contained in the error on the respective d spacing. The deviation between the two d spacings is due possibly either to a non-linearity in the sine-screw mechanism or a slightly improbable value quoted for the wavelength of one of the calibration lines.

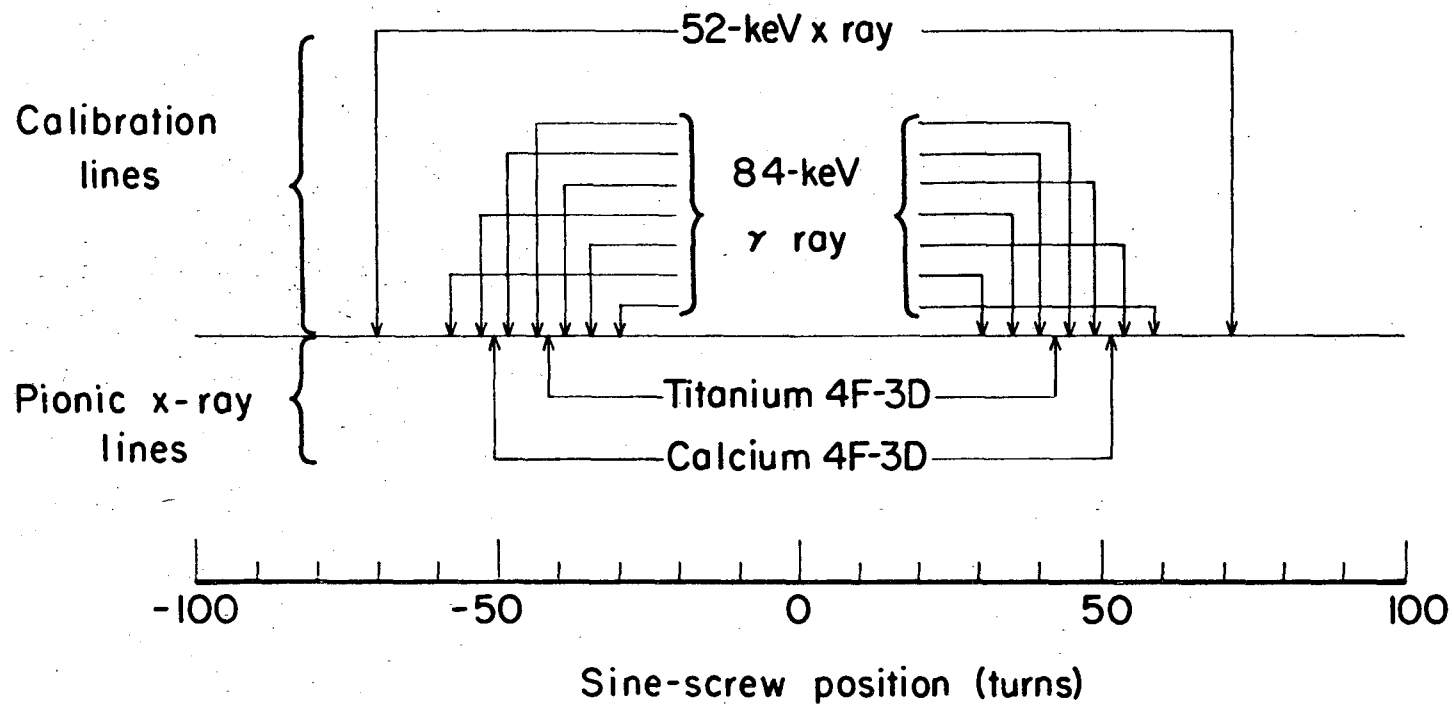The d spacing used for the pionic x-ray experiment is derived from the two calibration lines by a linear extrapolation, the d spacing thus being somewhat dependent on λ.

Thus

$$d(\lambda) = a + b\lambda = 1177.38 + 0.0008\lambda$$

$$\sigma^2(\lambda) = [0.00066 \,(237-\lambda)]^2 + [0.00033 \,(\lambda-147)]^2$$

[2]

In particular, for the wavelengths of the pionic x-rays to be measured:

Fig. 14:   Each pair of arrows indicates the location on the sine screw of a pair of diffraction
peaks.   The location of all the pairs of calibration peaks is illustrated.   Also shown
is the location of the 4 pionic x-ray diffraction peaks used in the pion mass measurement.

Transition	Wavelength	d_{18} Spacing
Titanium 4F-3D	141 xu	1177.49 ± 0.06 xu
Calcium 4F-3D	171 xu	1177.52 ± 0.05 xu

A one-point calibration (using the 84 keV x-ray) would of course yield a d spacing 0.03 xu lower for the calcium line. In order to prevent misinterpretation, such a shift would change the pion mass quoted in this paper by about 10 per cent of the assigned standard error.

III. PIONIC X RAYS

A. Introduction

Pionic and muonic x-rays have been studied for several reasons, including investigations into atomic physics, nuclear electromagnetic form factors, hyperfine structure effects, and the π-nuclear interaction. They have also been studied with the objective of measuring the pion and muon masses. Early mass measurements by this technique are discussed in several review articles.[33-35] One specific measurement of the pion mass is outlined in Part I of this paper.

In the previous mass measurements, the most precise method suitable for mesonic x-ray studies was the absorption-edge technique. As the absorption coefficient of an x-ray filter can vary by a large factor in a very small energy interval, precise limits could be placed on the x-ray energies.

Suspicion that the strong component of the 3D-2P muonic phosphorus x-ray lay directly on the 100 eV wide K absorption edge of lead prompted the most precise mesonic x-ray transition-energy calculation to date. In 1959, Petermann and Yamaguchi[36] calculated the quantum-electrodynamic corrections to the Dirac equation for the $3D_{5/2}$ and $2P_{3/2}$ levels of muonic phosphorus, yielding a relationship between the muonic x-ray energy and the muon mass with a precision of ± 25 ppm. Meanwhile, several experiments measured the absorption coefficient of these x rays in lead. Combination of these data yielded an estimate of the muon mass with a precision of ± 100 ppm which, when compared with a more recent independent measurement of the muon mass (with a precision of ± 15 ppm), verified the muonic x-ray calculations to ± 100 ppm.[11] There

is no reason to doubt, however, that the transition energy can be calculated to the ± 25 ppm error quoted.

The second-order (in e) corrections to the Dirac equation in muonic phosphorous fall into two distinct categories, the virtual production of electron-positron pairs by the Coulomb field (vacuum polarization), and the virtual emission and re-absorption of photons by the muon (Lamb shift). It is interesting to note that the Lamb shift in muonic phosphorous is a very small effect (~ 0.5 eV) compared to the vacuum polarization (~ 330 eV), which is certainly not the case in the $2S_{1/2}$ level in hydrogen, where the Lamb shift is some 40 times larger than the vacuum polarization.[37]

In the present experiment, the only important quantum-electrodynamic correction to the wave equation is the vacuum polarization term, which is a correction to the Coulomb field itself, and therefore does not depend directly on the intrinsic properties of the meson. This term has been adequately tested both in muonic phosphorous and the hydrogen atom.

There are, however, two important differences between muonic and pionic atoms which cannot be ignored. The pion is a spin 0 particle, and therefore the Dirac equation must be replaced by the Klein-Gordon equation. Furthermore, the pion is a strongly-interacting particle, and therefore its interaction with the nucleus produces effects on the energy levels typically two orders of magnitude larger than do the electromagnetic form factors.

B. Strong Interaction Shifts in Pionic Energy Levels

In 1954 Stearns et al.[38] discovered a repulsive shift in the 1S level of pionic beryllium. This was shortly followed by several papers,

both theoretical[39-43] and experimental,[44-46] on the effects of the π-nuclear interaction in pionic atoms. De Benedetti,[33] Stearns[34], and West,[35] review most of the work up to 1958. The 1S level shifts have been explored further in more recent theoretical papers,[47-50] although no further experimental work has been published.

Several authors[47,49,51] have derived estimates of the 2P level shift using pion-nucleon scattering lengths. As the dominant effect was expected to be from the large and positive 3-3 scattering length, these estimates predicted an attractive shift, which was contrary to existing experimental data.[45]

In 1955 Kisslinger[52] derived a velocity-dependent optical model to account for the large p wave interaction in π-nuclear scattering. In 1958 Baker et al.[53] used a modified Kisslinger potential in the analysis of π-nuclear scattering data with considerable success. Recently Ericson and Ericson[54-57] developed a velocity-dependent optical potential for pionic atoms from Kisslinger's potential, again predicting an attractive shift in the 2P level of pionic atoms, based on π-nucleon scattering lengths. In 1964 Astbury et al.[58] observed an attractive shift of -240 ± 80 eV in the 2P level of pionic aluminum using a bent crystal spectrometer. Very recently Jenkins[59] has observed attractive shifts in the 2P, 3D, and 4F levels of pionic atoms, as well as the expected repulsive shift in the 1S level, using a Ge(Li) detector.

The most recent paper by Ericson and Ericson[57] is a detailed discussion of level shifts and widths in pionic atoms. They have included multiple scattering, non-linear density effects, Fermi motion, nucleon-nucleon correlation, and the effect of nuclear absorption on the level shift. On substitution of s and p wave π-nucleon scattering

lengths they find reasonable agreement with the experimental data, although with some fairly large uncertainties.

In order to measure the pion mass by the mesonic x-ray technique, it is necessary to find a transition where the expected strong-interaction level shift is small. This can be done by using first-order perturbation theory in combination with the measured 2P shift in pionic aluminum.

The energy-level shift calculation is performed by using Ericson and Ericson's optical potential in perturbation theory form:

$$\Delta E = <\psi \mid V(r) \mid \psi> - \frac{\hbar^2}{2M_\pi} < \vec{\nabla} \psi \mid \alpha(r) \mid \vec{\nabla} \psi> \qquad [3]$$

where $\psi = \psi(\vec{r})$ is the unperturbed orbital wave function. The first term represents a standard local-interaction potential. In the second term, $\mid \vec{\nabla} \psi \mid$ may be recognized as the wave number $\mid \vec{k} \mid$, showing that the term represents a velocity-dependent (and hence non-local) potential. $V(r)$ and $\alpha(r)$ represent the effective "potentials", and for the purposes of this calculation are assumed to be finite and constant over the nuclear volume.

It should be noted that the non-local term vanishes for $\psi = 1S$ orbits (in perturbation theory at least), allowing the local term to dominate. Hence in this optical model, the local term is recognized as representing the repuslive potential observed in the 1S level, and non-local term is recognized as the attractive potential which appears to dominate in the 2P, 3D, and 4F levels.

In scaling from the aluminum 2P level to other levels, the depth of the potential is assumed to remain constant, and the nuclear radius to vary as $r_o A^{1/3}$. Consider the 3D level in pionic titanium for example. If r_o is assumed to be 1.1 Fermi and the -240 eV shift in the 2P level

of pionic aluminum is assumed to be due purely to a local potential, the level shift in the 3D state of titanium would be -3 eV. On the other hand, if the potential were assumed to be entirely non-local, the titanium level shift would be -5 eV. On the basis of all the available experimental data, Ericson and Ericson[57] estimate the -240 eV shift in aluminum to be a combination of +80 eV local and -320 eV non-local interaction. In this case the titanium level shift is estimated to be -6 eV.

By varying the radius of the square well in the perturbation calculation it is possible to estimate the sensitivity of the titanium shift to nuclear edge effects. The depth of the potential, however, is assumed to be the same in both the aluminum and titanium, and is varied only to match the measured shift. Mottershead[60] has estimated that the first-order perturbation-theory calculation yields a potential 30 per cent too deep for the 2P level shift in aluminum, since the wave function is underestimated. Considering these effects as well as the experimental errors, a shift of -4 ± 4 eV has been assigned to the 3D level of pionic titanium.

Jenkins'[59] data includes measurement of 2P level shifts for 15 < Z < 25, and 3D level shifts for 30 < Z < 50. Preliminary analysis indicates that the 2P level shifts are in agreement with the measured 2P shift in aluminum, and further that the ratio of 2P to 3D level shifts is consistent with the optical model. The tentative agreement of this data seems to indicate that there is no large anomalous Z or L dependence, and therefore the estimated -4 ± 4 eV shift in the 3D level of titanium seems to be reliable.[61]

The ± 4 eV error assigned to the expected shift in the titanium

4F-3D transition represents a fractional error of about $\pm$ 50 ppm. Hence it would be possible to measure the pion mass to $\pm$ 100 ppm using titanium. As perturbation theory indicates the strong interaction shift in the 3D level to vary as Z^9, and as the 4F-3D transition energy varies as Z^2, it is possible to measure the pion mass to $\pm$ 100 ppm precision using the 4F-3D transition for $Z \leqslant 22$.

C. Other Considerations

Since the lower limit for the bent crystal spectrometer is 40 keV, the choice of 4F-3D transitions is limited to the following six elements:

Element	Z	4F-3D Energy
Phosphorus	15	41 keV
Sulfur	16	46
Potassium	19	65
Calcium	20	72
Scandium	21	80
Titanium	22	88

Consideration was given to each of the following points in deciding which transitions to measure:

1. Energy dependence of spectrometer efficiency

2. Energy dependence of spectrometer resolution

3. Pionic x-ray yield[62] (the theoretical yield curves, at one time found to be in disagreement with experimental measurements,[63] are now in agreement[64])

4. Self-absorption coefficient for the x-rays in target

5. Stopping power of target material for pions (when the target is

1 mm or less thick this is an important consideration as it determines
the signal-to-noise ratio of the pion telescope)

6. The energy dependence of the background in the NaI detector

7. The energy dependence of the energy resolution of the NaI
detector

8. The energy dependence of the jitter in the NaI timing signal.

Points 5,6,7, and 8 are only important when background is a
problem. As a signal-to-noise ratio between 1 and 2 was expected in
this experiment, these points were an important consideration (see
Equation A-6 for example).

Based on these points, the 4F-3D transition of titanium seemed
to be optimum. Although scandium was the second choice, calcium was
chosen instead, since any anomalous Z dependence of the pion mass
measurement would be more apparent.

D. Energy Level Calculations

The evaluation of the pionic 4F-3D transition energies in calcium
and titanium is summarized in Table II. As the expected experimental
precision is of the order of 10 eV, all calculations are expressed to
the nearest eV.

These calculations are based on an origin value of 139.580 MeV
for the π^- mass. The origin value, divided by the calculated transition
energies, yields scale factors which to a good approximation are in-
dependent of the origin value. Specifically, a 1 MeV shift on the origin
value is expected to produce only a 30 ppm effect on the scale factor.

As pions have no spin, the relativistic Schrodinger (Klein
Gordon) equation for a central Coulomb field, described in Section 42

Table II. Calculation of the 4F-3D Pionic Calcium and Titanium Transition Energies Using $M_\pi c^2$ = 139.580 MeV.

Effect	Calcium	Titanium
Klein-Gordon Equation	72.388 ± 0.001 keV	87.622 ± 0.001 keV
Reduced Mass	- 0.270 ± 0.001	- 0.273 ± 0.001
Vacuum Polarization (Second-Order)	+ 0.230 ± 0.002	+ 0.301 ± 0.002
Vacuum Polarization (Fourth-Order)	+ 0.002 ± 0.002	+ 0.002 ± 0.002
Strong-Interaction Shift	+ 0.002 ± 0.002	+ 0.004 ± 0.004
Orbital-Electron Screening	- 0.001 ± 0.001	- 0.001 ± 0.001
Electromagnetic Form Factors	negligible	negligible
Lamb Shift	negligible	negligible
π-Atomic Recoil	negligible	negligible
Calculated Transition Energy	72.351 ± 0.004 keV	87.655 ± 0.005 keV
Scale Factor: $\dfrac{M_\pi c^2}{\text{Transition Energy}}$	1929.21 ± 55 ppm	1592.38 ± 57 ppm

of Schiff,[65] is used. To insure the required precision, the exact

solution for the energy levels is used by expanding it in a binomial

series and retaining the required number of terms. The expression

$$W(n,\ell) = -\left[\frac{1}{2}\left(\frac{\gamma}{\lambda}\right)^2 - \frac{3}{8}\left(\frac{\gamma}{\lambda}\right)^4 + \frac{5}{16}\left(\frac{\gamma}{\lambda}\right)^6\right] M_\pi c^2, \qquad [4]$$

where $\gamma = \alpha Z$ and $\lambda = (n-1)-\ell + 1/2 + [(\ell + 1/2)^2 - \gamma^2]^{1/2}$, has sufficient

precision for the levels in question. The value $1/\alpha = 137.0388 \pm 4$ ppm[66]

was used, its error producing the ± 1 eV error on the calculated

transition energies (note that by using the fine structure constant,

the π^- charge is hereby assumed to be the same as the electronic charge).

In the case of titanium, the relativistic shift in the transition energy

is about +187 eV.

The reduced mass correction is[67]:

$$E = \frac{W}{1 + M_\pi / M_N} - \left(\frac{Z\alpha}{2n}\right)^2 \cdot (M_\pi/M_N) \cdot |W|, \qquad [5]$$

where W = energy defined in Equation [4], E = "reduced" energy, and

(M_π/M_N) is the pion-to-nuclear mass ratio. Note that E and W are both

negative energies. The nuclear motion term, a 0.5 eV effect, is ex-

pected to be the largest correction to the standard reduced mass

evaluation. In the case of titanium, where about 25 per cent of the

nuclei have A = 46, 47, 49 or 50 (75 per cent is A = 48), five distinct

lines are produced in an energy band about 20 eV wide. As this band

is about 10 per cent of the experimental resolution and about 7 per

cent of the reduced mass correction, the effect of the splitting on

the analysis is negligible.

Polarization of the virtual electron-positron pairs produced

in the Coulomb field of the nucleus can cause, at distances of the order

of or less than the electron Compton wavelength $\hbar/mc \sim 390$ Fermi, noticeable deviations from the classical Coulomb potential. This effect, usually referred to as vacuum polarization, was first calculated by Uehling[68] in 1935. This calculation has been checked to ± 1 per cent in the hydrogen atom[37] and to ± 3 per cent in muonic phosphorous (see Section III A). For the energy levels of interest here, $< r >$ is in the range 80 to 140 Fermi, and the corresponding vacuum polarization corrections to the energy levels are in the range 0.1 to 0.2 per cent.

Several authors[69-71] have estimated the second-order vacuum polarization effect in mesonic atoms using the Uehling integral in a first-order perturbation-theory calculation with non-relativistic orbital wave functions. In Appendix B this calculation is carried out using relativistic wave functions, yielding a +229.0 eV shift for calcium and a +299.7 eV shift for titanium. Wichmann and Kroll[72] have calculated the corrections to the Uehling integral, and demonstrate that they give rise to an additional shift $\Delta E < 1.9 \times 10^{-8} \ Z^2 \cdot E$, hence < 0.8 eV for titanium. Glauber et al.[73] have corrected the first-order perturbation-theory calculation for the perturbation on the orbital wave function, and find less than a 1 eV effect on the 329 eV vacuum polarization shift in muonic phosphorous. The effect should be quite similar in the pionic atoms considered here. The total second-order vacuum-polarization effect is estimated to be 230 ± 2 eV for calcium, and 301 ± 2 eV for titanium.

The fourth-order vacuum polarization effect has been calculated by Petermann and Yamaguchi[36] to be approximately 2.9 (α/π) times the second-order effect in muonic phosphorous. By comparison, the ratio in the hydrogen atom[74] is 3.8 (α/π). Assuming the ratio to be about

2.9 (α/π) for the pionic transitions yields a +2 ± 2 eV shift in both calcium and titanium.

As discussed in Section III B, the strong interaction shift is estimated to be +4 ± 4 eV for titanium, and +2 ± 2 eV for calcium.

The short-range electromagnetic effects, including the pion and nuclear form factors, and the Lamb shift, are approximately 2 orders of magnitude smaller than the strong interaction shift and therefore negligible.

Recoil of the pionic atom following the x-ray emission is a -0.1 eV effect and therefore also negligible.

The effect of atomic electrons penetrating the region of the pionic orbit is easily estimated assuming that the probability density of the two 1S electrons is a constant in the region of interest. The level shift in the pionic atom, relative to the origin, produced by two 1S electrons, is:

$$\Delta E \simeq \frac{-4}{3} \; e^2 \; (\frac{Z-1}{a_o})^3 < r^2 > \qquad [6]$$

where for pionic atoms

$$< r^2 > \; = \; 126 \; (a_\pi/Z)^2 \qquad \text{3D level}$$

$$= \; 360 \; (a_\pi/Z)^2 \qquad \text{4F level}$$

In these expressions a_o and a_π represent the electronic and pionic Bohr radii, and the factor $(e^2/a_o) = 27.2$ eV. The overall effect is to decrease the transition energy (since $\vec{E}(r)$ is reduced everywhere, so is $|dV/dr|$).

In the calcium and titanium transitions this would be a -2 eV effect. However, as the pionic 4F-3D transition is considerably faster than the electronic 2P-1S (E1 radiative transition rates, listed in

Condon and Shortley,[75] are linear in mass x Z^4), vacancies produced by previous pionic Auger transitions will probably not be filled in time. Rather than calculate this, the electronic screening is instead estimated to be -1 ± 1eV.

Natural linewidths are of the order of several eV, the main contributions coming from the 3D-2P E1 transition rates and nuclear absorption of pions from the 3D level. They are expected to be the symmetric Breit-Wigner resonance curves, and therefore do not affect the transition energies.

A similar calculation has been carried out for the 4D-3P transition in calcium, and it is found that the effects of the relativistic fine structure, the vacuum polarization, and the π-nuclear interaction, are all additive and shift the energy at least 1 keV relative to the 4F-3D transition (the spectrometer resolution is about 140 eV). Furthermore, Jenkins'[59] data tentatively indicates the 4D-2P intensity to be about 15 per cent (within a factor of 2) of the 4F-3D in calcium, indicating that the 4D-3P yield is about 5 per cent of the 4F-3D. Therefore, in the data analysis only the 4F-3D line will be assumed to be present.

IV. THE EXPERIMENT

A. The Pion Beam

The arrangement of the π^- beam transport system is shown in Figure 15. The pions, produced on an internal beryllium target by the 730 MeV circulating proton beam, were momentum analyzed by the Cyclotron magnet, and then focused at infinity by Q1. The beam was again momentum analyzed by H1 and then focused by Q2. The optics in the horizontal plane (Q1a, Q1b, H1, Q2a, Q2b) were FDODF.

The objective in setting up this beam was to obtain a maximum density of stopping pions in the region of the focus. Before H1 was set in place, a five-counter pion telescope was placed at the exit end of the meson wheel to measure stopping-pion rates in a thin target, as a function of wheel angle and internal target position. The meson wheel was stopped down to a 1.5" x 2" aperture at each end, and an automated range-changing device was used. A total of about 80 range curves at 6 wheel angles were measured to insure that both the wheel orientation and the internal target position were optimized.

With the magnets in place and the stops removed, the optimized pion momentum was determined to be about 180 MeV/c with a momentum spread (fwhm) of $\Delta p/p = 7$ per cent (this corresponds to E $\sim$ 90 MeV and $\Delta E/E \sim 10$ per cent). The total beam intensity penetrating at least 16 g/cm^2 of CH_2 was observed to be about 1.5×10^6/sec. (This was the maximum. The experiment was performed at the beam level of 1.0×10^6/sec which could be consistently extracted from the Cyclotron). Contamination due to μ's and e's was in the range of 30 per cent to 40 per cent.

Q2 was placed as close as possible to second focus to minimize the image distance in the horizontal plane(the distance from the center
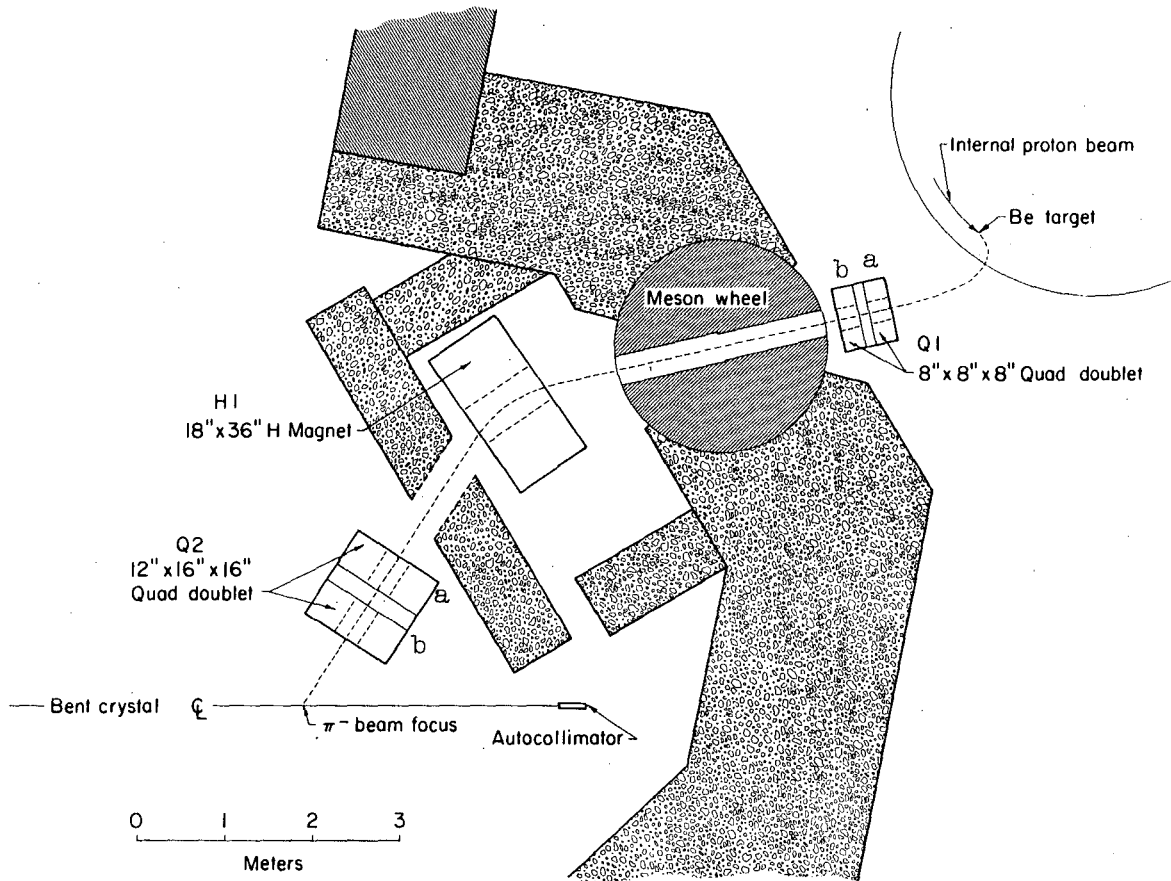
Fig. 15: The π^- beam transport system.

of Q2b to the focus was about 110 cm). The cross section of the beam (after penetrating approximately 20 g/cm^2 of CH$_2$) was about 4 cm wide and 13 cm high. The width of the differential range curve for pions was about 3.5 g/cm^2 of CH$_2$ (fwhm).

The microscopic duty cycle was about 20 per cent on a 52 nsec time base, the macroscopic duty cycle of useable beam was about 60 per cent on a 16 msec time base. Thus there were about 11 x 10^6 rf cycles of beam per second or an average of 1 particle every 11 rf cycles.

B.   The Experimental Arrangement

The overall experimental arrangement is outlined in Figure 16. The incoming pion beam was analyzed by pion telescope as it stopped in the region of the mesonic x-ray target. An autocollimator defined a line of sight on which the mesonic x-ray target was placed. A NaI(Tℓ) detector behind the bent crystal detected the diffracted x-rays.

As is indicated in Table I, the intrinsic resolution of the spectrometer at the focus is approximately 0.6 mm (fwhm). The objective of the experiment is to measure the diffraction angle of the pionic x-rays with a precision comparable to a small fraction of the instrumental resolution, hence requiring stability of the target position within approximately 0.05 mm (as will be seen,however, knowledge of its position is not nearly as important). Such a tolerance must be assured over the entire duration of the experiment, which represents a period of several weeks.

As has already been mentioned, the bent crystal spectrometer is mounted on a concrete foundation. The foundation of the autocollimator was a six-ton concrete block grouted to the concrete floor of the
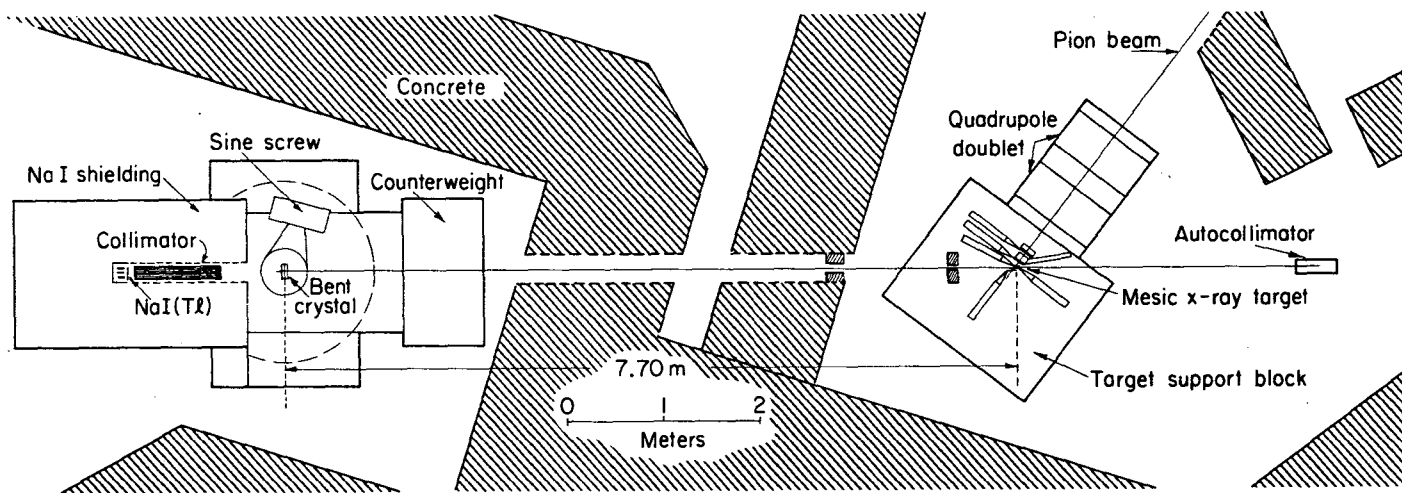
Fig. 16: The experimental arrangement. The incoming pion beam is analyzed by a pion telescope as it stops in the region of the mesonic x-ray target. An autocollimator defines the bent crystal centerline. The diffracted x-rays are detected with a NaI(Tℓ) detector, which is in coincidence with the pion telescope.

experimental area. In addition, the pionic x-ray target and pion counter telescope were themselves mounted on a similar concrete block.

The autocollimator was a high-resolving-power alignment-telescope[76] with an optical micrometer, capable of autoreflection and auto-collimation on a mirrored surface. The line-of-sight distance to the bent crystal was about 10 meters. Mounted permanently on the bent-crystal form-block directly in front of the central rib (see Figure 7) was a hardened-steel bar whose front surface was ground and lapped flat. Centrally located on this was a 1 cm diameter optical-alignment target, and around this a removable front-surface mirror six cm in diameter could be attached. The pionic x-ray target, approximately 762 cm from the bent crystal axis of rotation, was suspended from a micrometer stage (note in Figure 1 that the focal length is the focal-circle diameter times the cosine of the Bragg angle).

The bent-crystal centerline was defined by the autocollimator benchrest and the center of the alignment target on the bent-crystal form block. This line of sight could be checked with the optical micro-meter. Typically it would repeat within ± 0.05 mm (a single measurement is the average of several observations). The mirror could be rotated into autocollimation with the sine-screw mechanism to check the spect-rometer alignment. Generally this would repeat within ± 3 seconds of arc. The optical micrometer could also be used for checking the pionic x-ray target position relative to the line of sight. This usually repeated within about ± 0.04 mm.

It is not known whether the above deviations represent mechanical motion of the experimental equipment or observational errors. In this respect it is worthwhile to refer to the four points in the center of

Figure 13, which required about an hour apiece to measure. If their external consistency were due entirely to mechanical motion of the source (and not counting statistics or temperature effects in the quartz) it would indicate a rms deviation of ± 0.003 mm for each one-hour period. This is well beyond the capability of the optical micrometer. The methods used to minimize possible errors from mechanical motion will be described in the section on experimental procedure.

The pion telescope is shown in Figure 17. Counters 1 and 2 monitored the incident beam. The stopping particle was defined by counter logic $123\overline{45}\overline{C}$. Both 3 and 4 used thin (0.8 mm) Pilot B scintillators, backed with lucite for increased light collection efficiency. The thin scintillators were required to minimize the target-out stopping rate, as the background in this experiment was proportional to the gross stopping rate, while the yield of pionic x-rays was proportional to the net stopping rate in the target. Furthermore, counter 3 could be voltage-plateaued so as to have a high efficiency for slow, heavily-ionizing pions, and a relatively low sensitivity to minimum ionizing particles. Counter 4 was designed to be efficient for pions with only a small residual range, while counter 5 detected the fast minimum-ionizing particles missed by 4. This combination of two anti-counters resulted in about 30 per cent lower target-out rate than could be obtained by a single anti-counter. The Čerenkov counter was used to reduce erroneous $123\overline{45}$ signals due to electrons. The degrader shown in Figure 17 represents a total of about 22 g/cm^2 of CH_2, lucite, and scintillator.

The dimensions of the pionic x-ray target required careful consideration, as they influenced the total events rate, the accidental
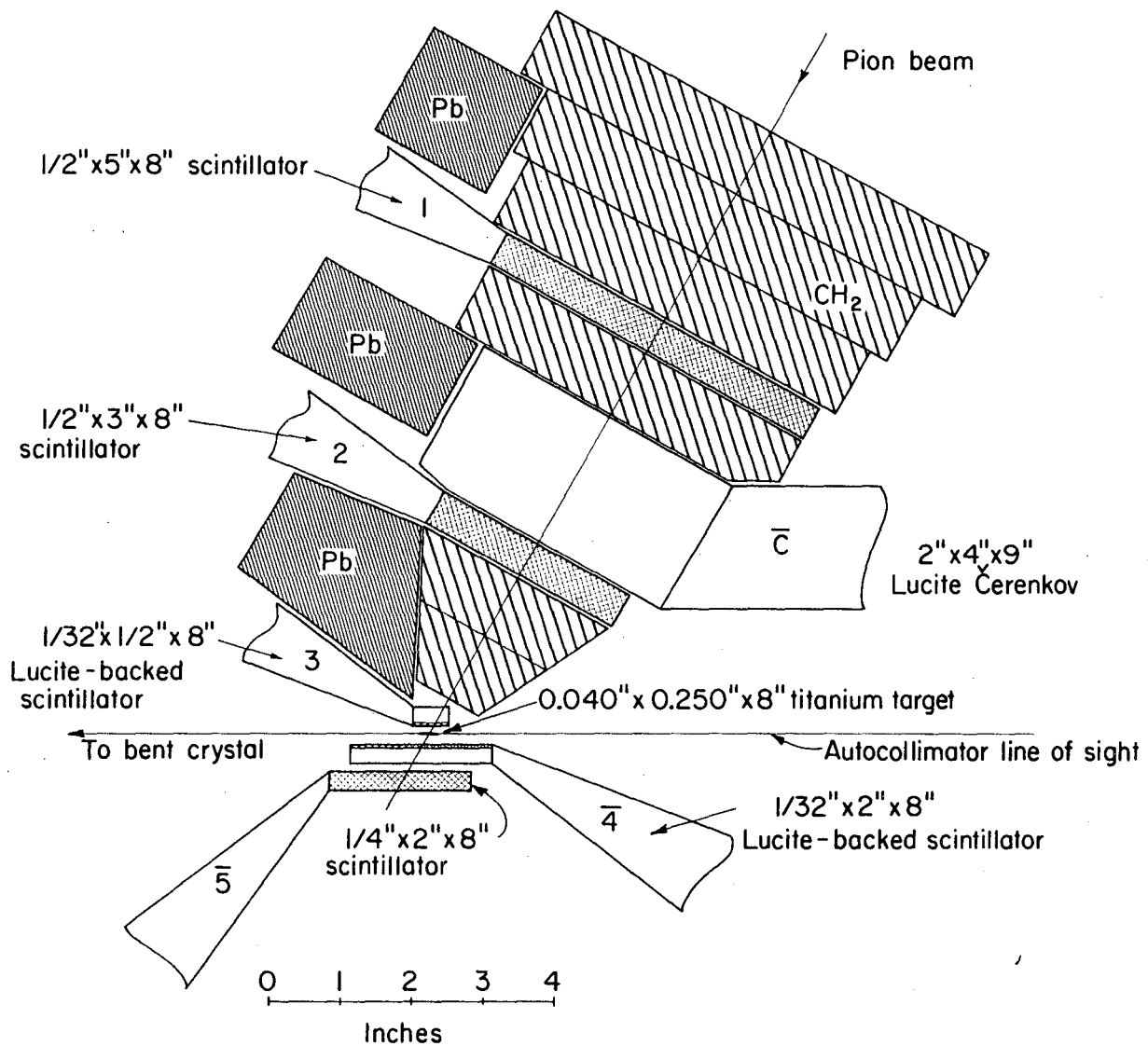
Fig. 17: The pion counter-telescope arrangement. A stopping pion was identified by a 123$\overline{4}\overline{5}\overline{C}$ logic requirement.

coincidence rate, and the experimental resolution. The dimensions are:

    a: the dimension in the diffraction plane normal to the bent crystal centerline

    b: the dimension in the diffraction plane parallel to the bent crystal centerline

    c: the dimension normal to the diffraction plane.

The ability of the target to stop pions is approximately proportional to its gram/cm^2 times its area normal to the beam, hence its mass. If dimension "a" is comparable to or larger than the spectrometer resolution (0.63 mm as indicated in Table I), or if dimension "b" is comparable to or larger than a pionic x-ray absorption length, then the overall efficiency is affected. After a detailed consideration of these effects, the pionic x-ray targets were designed with the dimensions:

    a = 1.0 mm

    b = 0.8 absorption lengths (12.5 mm for Ca, 6.5 mm for Ti)

    c = 200 mm

These were estimated on the basis that the signal-to-noise ratio of the final data would be between 1 and 2 (as will be seen, this was slightly optimistic). Dimension "a" is actually a little larger than would be estimated on the basis of Equation A-6, as some precision was sacrificed for an increased ability to discriminate against background (i.e. a somewhat broader resolution, but containing more events).

It is now possible to estimate the total system efficiency. The factors influencing the efficiency for the titanium 4F-3D x-ray are:

        Intrinsic efficiency of spectrometer (Figure 11)   1.3 x 10^{-6}

        x-ray yield (production)[62]   0.5

        Self-absorption in target   0.7

Target width	0.7
NaI detector efficiency	0.9
Other effects (data accumulation and analysis)	0.7
Overall efficiency	$\sim 2 \times 10^{-7}$
	events/stopping π

The entry "Other effects" corresponds to sacrificing a little signal to obtain a more-than-compensating increase in the signal-to-noise ratio. As the diffracted x-rays detected by the NaI are localized in both time (by coincidence with the pion telescope) and energy (pulse-height analysis), the x-rays produced a bivariate distribution in energy-time space. The background, however, showed no time dependence and very little energy dependence. Discrimination against background was performed by selecting out a small region of space centered on the bivariate distribution. The dimensions of this region determined the signal rate, as well as the signal-to-noise ratio, of the selected data. The effect of these two parameters on localizing the mean of the diffraction peaks may be estimated from Equation [A-6].

Diffraction of the 84.261 keV calibration line into the $NaI(T\ell)$ detector yielded a resolution of 25 keV (fwhm). This corresponds statistically to $< N > = 63$ photoelectrons approximately. Sampling the leading edge of the $NaI(T\ell)$ pulse should yield the best timing resolution.[77] If the timing resolution is due entirely to the photoelectron statistics then the resolution should be approximately[78]

$$\delta t = \frac{\sqrt{n} \ \tau}{< N >} \quad (rms) \qquad [7]$$

where $\tau = NaI(T\ell)$ decay constant $= 200$ nsec, and $n/N =$ fraction of pulse sampled. In particular, for the 88 keV titanium transition

$$\Delta t = \frac{2.35 \times 200}{66} = 7 \ nsec \ (fwhm) \qquad [8]$$

based on sampling the first photoelectron [admittedly, the ratio (fwhm/rms)= 2.35 is a poor approximation for n = 1]. Assuming the pion telescope resolution to be about 4 nsec (fwhm), the total timing resolution will be about 8 nsec. Based on < N > = 66 photoelectrons, the pulse height resolution will be about ΔE = 26 keV (fwhm) for the 88 keV x-ray.

If the pulse height and timing windows are both about 1.5 fwhm wide, and about 50 per cent of the $123\bar{4}\bar{5}\bar{C}$ pulses correspond to pions stopping in the titanium target, the total "phase space" per stopping pion is $(1.5 \times 8 \times 10^{-9}$ sec) $\times (1.5 \cdot 26$ keV) $\times$ 2 = 9.4×10^{-7} keV-sec/ stopping pion. The background in the NaI(Tℓ) was indicated in Section IIB to be about 0.09 events/keV-sec. So the total background rate in this experiment should be 0.09 $\times$ 9.4 $\times 10^{-7}$ = 0.8 $\times 10^{-7}$ events/stopping pion.

C. The Electronics

A block diagram of the electronics is shown in Figure 18. Most of the modules are described in the UCRL Counting Handbook.[79] All of the photomultipliers used in the experiment were RCA 6810A tubes, the six tubes in the pion telescope being voltage-stabilized.

The resolution of the 123 coincidence was about 4 nsec (fwhm). On the output of this coincidence, a high-level discriminator was used to gate a low-level tunnel diode discriminator, thus standardizing the timing pulse with a minimum amount of jitter.

The nine photomultipliers on the NaI(Tℓ) were added linearly in an emitter-follower circuit. A standardized timing signal was derived from the leading edge of the pulse with a tunnel diode discriminator. As the discriminator typically fired many times during the scintillation, a univibrator in an anti-coincidence circuit was used to block pulses
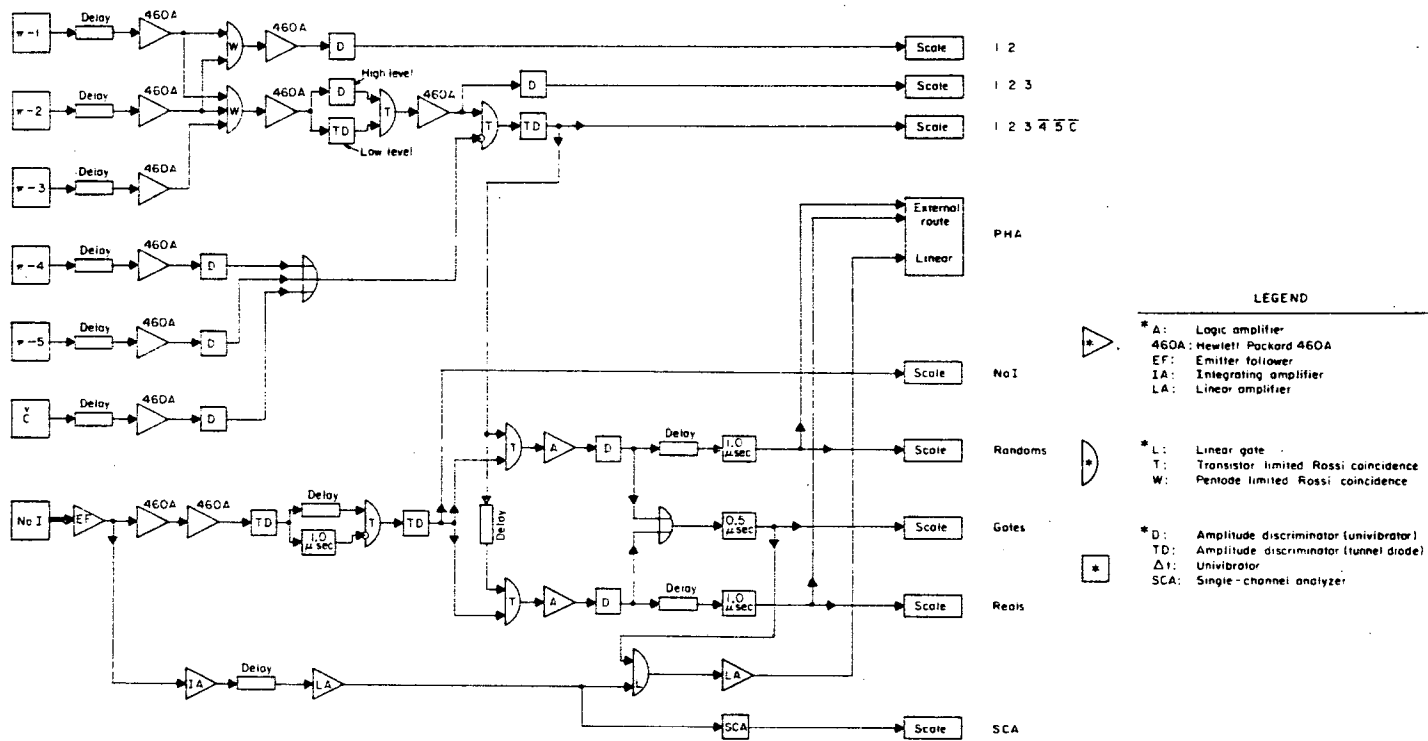
Fig. 18: Block diagram of electronic logic.

for 1 μsec after every time the discriminator fired. The NaI(Tℓ) pulse

was also processed for pulse-height analysis. Although tube-noise pulses

can trigger the timing discriminator, they originate from a small number of

photoelectrons. Therefore, when they are integrated for pulse-height analy-

sis, their pulse-height corresponds to that of a low energy (< 10 keV) x-ray,

which is easily distinguishable from the diffracted (70-90 keV) x-rays.

Two essentially identical coincidence circuits registered coin-

cidences between the pion-telescope and the NaI(Tℓ), the only differe-

nce being that the "Reals" circuit was timed to detect diffracted pionic

x-rays, and the "Randoms" circuit was off-delay by 2 Cyclotron rf cycles

(105 nsec). The generated external-routing pulses addressed the PHA in

binary logic (i.e. 00, 01, 10, 11) and the linear signal was routed

accordingly. Essentially all of the linear signals were accompanied by

a 01 or 10 command, the 11 being reserved for ambiguous coincidences

(i.e. two pions stopping 105 nsec apart).

As the long-term stability of the electronics was important, a

considerable amount of redundant information was derived from the circuit in

order to monitor discriminator levels, anti-coincidence efficiencies, and

the resolving time of the "Reals" and "Randoms" coincidence modules.

The "Reals" coincidence unit was set to the proper delay and

resolving time by pointing the bent crystal collimator directly at the

x-ray target rather than at the virtual image (see Figure 1), and addressing

the PHA with a time-to-height converter. The PHA was then externally

routed by both a single channel analyzer and the "Reals" coincidence cir-

cuit. The observed timing-resolution between the NaI(Tℓ) and $12\overline{3}4\overline{5}\overline{C}$ was

about 9 nsec (fwhm) and the resolving time of both the "Reals" and

"Randoms coincidence modules was adjusted to 14 nsec.

Typical average counting rates during the experiment were:

Scaler	Counts/sec (average)
12	1×10^6
123	5×10^4
$123\bar{4}\bar{5}\bar{C}$	1×10^4
NaI	8×10^3
Randoms	1.5
Reals	1.5
Gates	3
SCA	3.5

The reader is referred to Figure 18 for the definition of these terms.

D. Experimental Procedure

The procedure used in measuring the pionic x-ray wavelengths was
to scan alternately the regions where the right and left diffraction peaks
were expected to be, based on the transition energy calculations. As the
angular separation of the two diffraction peaks is completely determined
by the sine-screw mechanism, no reference to the line of sight was required
for the wavelength measurement. Knowledge of the target position was
required within approximately $\pm$ 0.2 mm, however, to insure that the
diffraction peaks were located well within the regions scanned. This
alignment was done with the calibration source.

The possibility of target motion has already been discussed. As
was indicated, short-term stability was excellent. It was necessary, how-
ever, to take some precautions so that unexpected or unobserved misalignments
would not affect this data.

The only suspected cyclic deviations in the alignment would be due to
temperature variations, which generally occur on a 24 hour cycle. For
this reason, and also because the Cyclotron crew rotates with the
same period, the spectrometer was operated on a 36 to 48 hour cycle, so

that over a period of many cycles, any effect of the suspected cyclic motion on the data would be minimized. No cyclic motion was observed during the experiment however.

The other possibility, of course, was an abrupt misalignment (earthquake, etc.). If such a misalignment were too small to be observed, then averaging over many cycles would make its contribution negligible. If the misalignment were observable, then analyzing the "before" and "after" cycles as independent measurements should completely eliminate its effect.

There is a possibility that a slight earth tremor caused a small misalignment during the calcium measurement. The effect was not large enough to be clearly discernable with the autocollimator, however, and no observable effect was seen when the data was analyzed.

As was pointed out in Section IIC, the thermal expansion coefficient of the quartz d spacing is about 15 ppm/$^\circ$C (to be compared with the final error on the pion mass measurement of $\pm$ 100 ppm). Therefore the ambient temperature near the bent crystal was recorded at periodic intervals. The average temperatures for the titanium and calcium experiments were 18.8°C and 19.5°C respectively, and the rms temperature variations were about $\pm$ 2°C. As the rms temperature variation was small compared to the final precision of the pion mass measurement, only a correction for the average temperature deviation from 18°C (the temperature at which Equation [2] is valid) was considered necessary in the data analysis.

As was indicated in Section IVA, the consistently obtainable beam level in the 12 coincidence (see Figures 17 and 18) was about

1×10^6 particles/sec, of which about 65 per cent were pions. The 123456 rate was monitored on a chart recorder, and held within ± 10 per cent of the proper value by the Cyclotron crew. The net stopping pion rates in the pionic x-ray targets were about 4,200 pions/sec in the titanium and 3,200 pions/sec in the calcium, based on target-in-minus-target-out rates and differential-range curves. As the titanium and calcium targets weighed approximately six grams and four grams respectively, the stopping pion rate was about 750 pions/gram-sec for each target.

Periodic checks were made on the electronics, including the NaI detector pulse-height response to a radioactive source insertable through the radiation shielding, and the pulse height analyzer operation including the external routing equipment.

As the data accumulation progressed, χ^2 analysis was able to estimate with reasonable precision the location of the diffraction peaks. Some additional effort was then concentrated on the points which localize the peak most effectively (differentiate Equation [A-3] as their location is a function of the signal-to-noise ratio) and an equivalent effort on the mode to discriminate against a straight-line fit.

The data thus obtained are displayed in Figures 19 and 20. The ordinate represents the events per 10^7 stopping pions in the target and the absicissae represent the diffraction peak locations in units of sine-screw turns from the mechanical center (1 sine-screw turn corresponds approximately to 3.345 xu). From the net stopping pion rates already discussed, it is seen that approximately 1.5×10^7 pions/hour could be stopped in the titanium target, and about 1.2×10^7 pions/hour in the calcium.
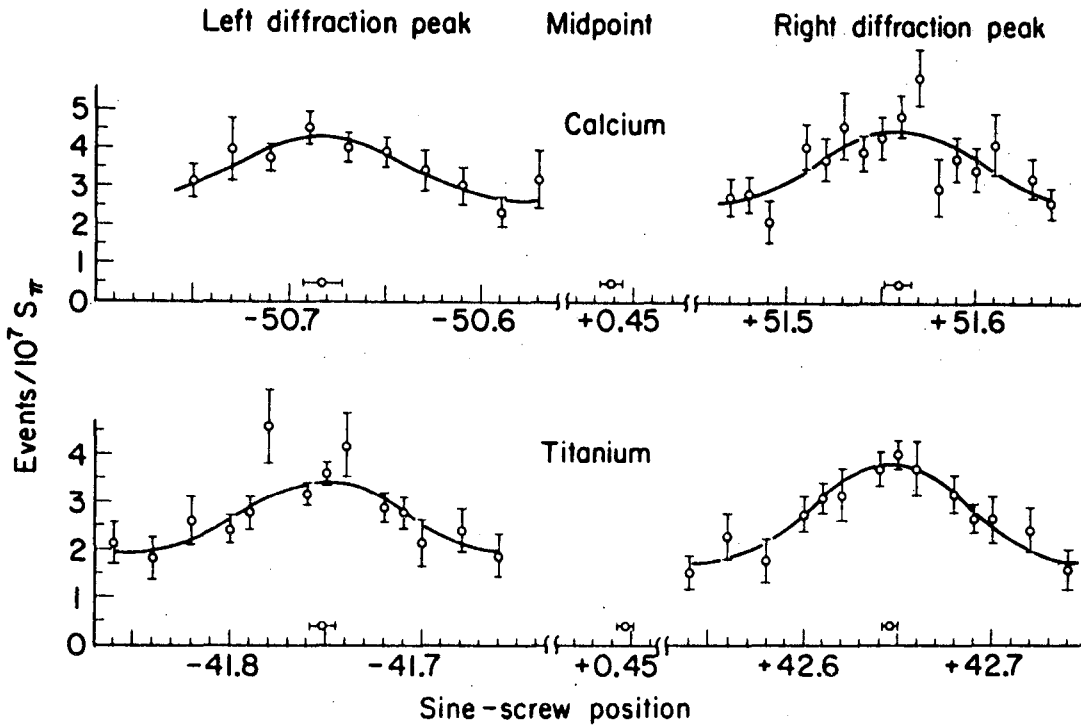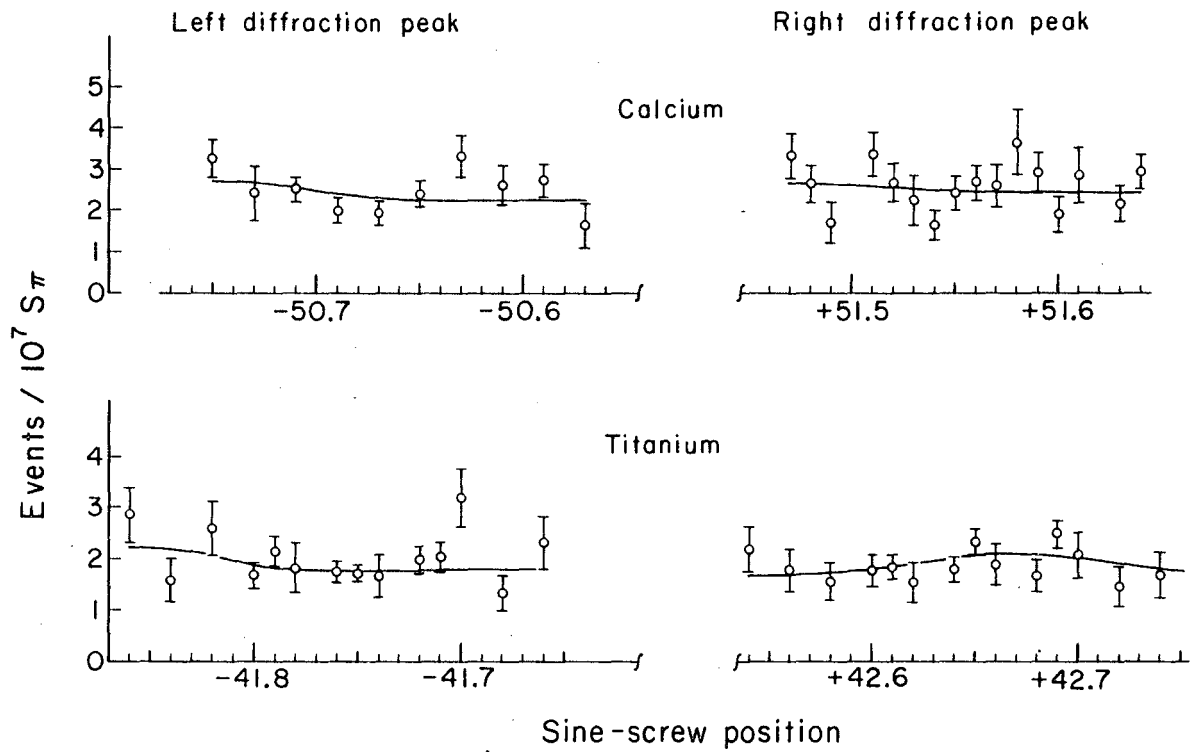
Fig. 19: The "Reals" data, plotted as the events rate vs. the sine-screw position, measured in units of screw turns from the mechanical center. The smooth curves are maximum likelihood estimates, and the horizontal error flags represent the results of χ^2 analysis.

Fig. 20: The "Random" data, plotted as the events rate vs. the sine-screw
position. The smooth curves are maximum likelihood estimates.

E. Data Analysis

The experimental resolution,

$$f(x-x_0) = [1 + \left[\frac{x-x_0}{b}\right]^2 - \left[\frac{x-x_0}{c}\right]^4] \exp \left[\frac{-1}{2}\left[\frac{x-x_0}{s}\right]^2\right] \qquad [9]$$

is the convolution integral of the intrinsic instrumental resolution

$$g(x-x_0) = \exp \left[\frac{-1}{2}\left[\frac{x-x_0}{\sigma}\right]^2\right] \qquad [10]$$

and a rectangle of width "a" representing the source width, where the constants are:

$$\sigma = 0.268 \text{ mm}$$

$$a = 1.00 \text{ mm}$$

$$b = 0.812 \text{ mm}$$

$$c = 0.930 \text{ mm}$$

$$s = 0.366 \text{ mm}$$

The conversion from millimeters to sine-screw turns is: 1 turn $\cong$ 10.82 mm. The experimental resolution is about 0.33 xu for each x-ray, which corresponds to 0.193 per cent (140 eV) for the calcium transition and 0.237 per cent (210 eV) for the titanium transition (fwhm). The expected experimental counting rate is of the form:

$$R(x-x_0 ; B, H) = B + H \cdot f(x-x_0) \qquad [11]$$

where B is the background level and H is the height of the mode of the diffraction peak.

In the data analysis, the function

$$\chi^2(x_0;B,H) = \sum_i \left[\frac{R(x_i-x_0; B,H) - Y(x_i)}{\sigma_i}\right]^2 \qquad [12]$$

where $Y(x_i) \pm \sigma_i$ is the mean and standard deviation of the i<u>th</u> experimental point, is minimized for each value of the independent variable x_o, with the restriction that $B \geqslant 0$ and $H \geqslant 0$. The resultant $\chi^2(x_o)$ is plotted as a function of x_o in Figures 21 and 22.

The sum of the minimum χ^2 for all the curves in Figure 21 is 31, and for Figure 22 it is 57. These are to be compared with the expected value of $< \chi^2> \pm \sqrt{2 <\chi^2>} = 42 \pm 9$.

If a straight line fit is attempted (i.e. $H = 0$), then the minimum χ^2 for the two figures is 159 and 66 respectively, to be compared with the expected value of 46 ± 10.

The only obvious disagreement is with a straight-line fit to the "Reals" data in Figure 19. The other χ^2 values, although not as nearly optimum as one would like, are nevertheless acceptable.

The magnitude of the deviations of these three χ^2 from their expectation values may be visualized in the following manner. If Birge's[80] external-to-internal consistency ratio is forced to the value 1 by modifying the magnitude of the internal errors, then for the "Reals" data, the internal errors would have to be decreased approximately 16 per cent, while for the "Randoms" data, the internal errors would have to be increased about 18 per cent. In essence, the standard deviation of the mean of the diffraction peaks, if based on internal consistency, would be about 16 per cent larger than the estimate based on external consistency. The more conservative estimate, based on internal consistency, will be used here.

The relative likelihood distributions for the four diffraction peaks, based on internal consistency, are plotted in Figure 23. The horizontal error flags represent the assigned standard deviations, and
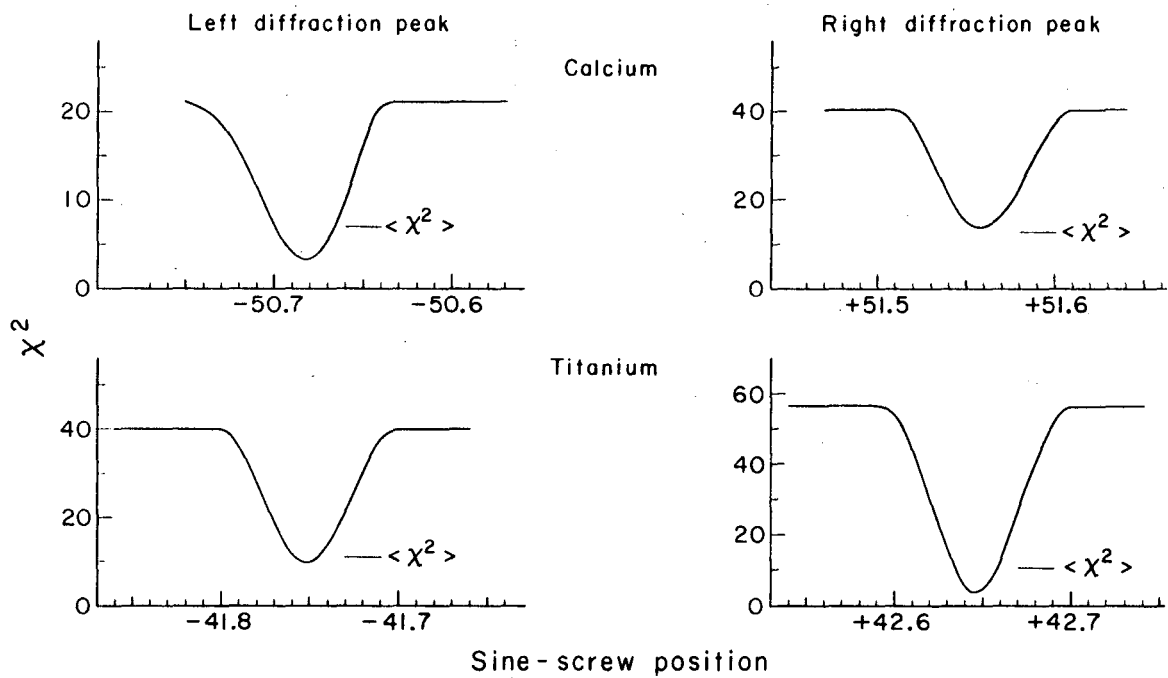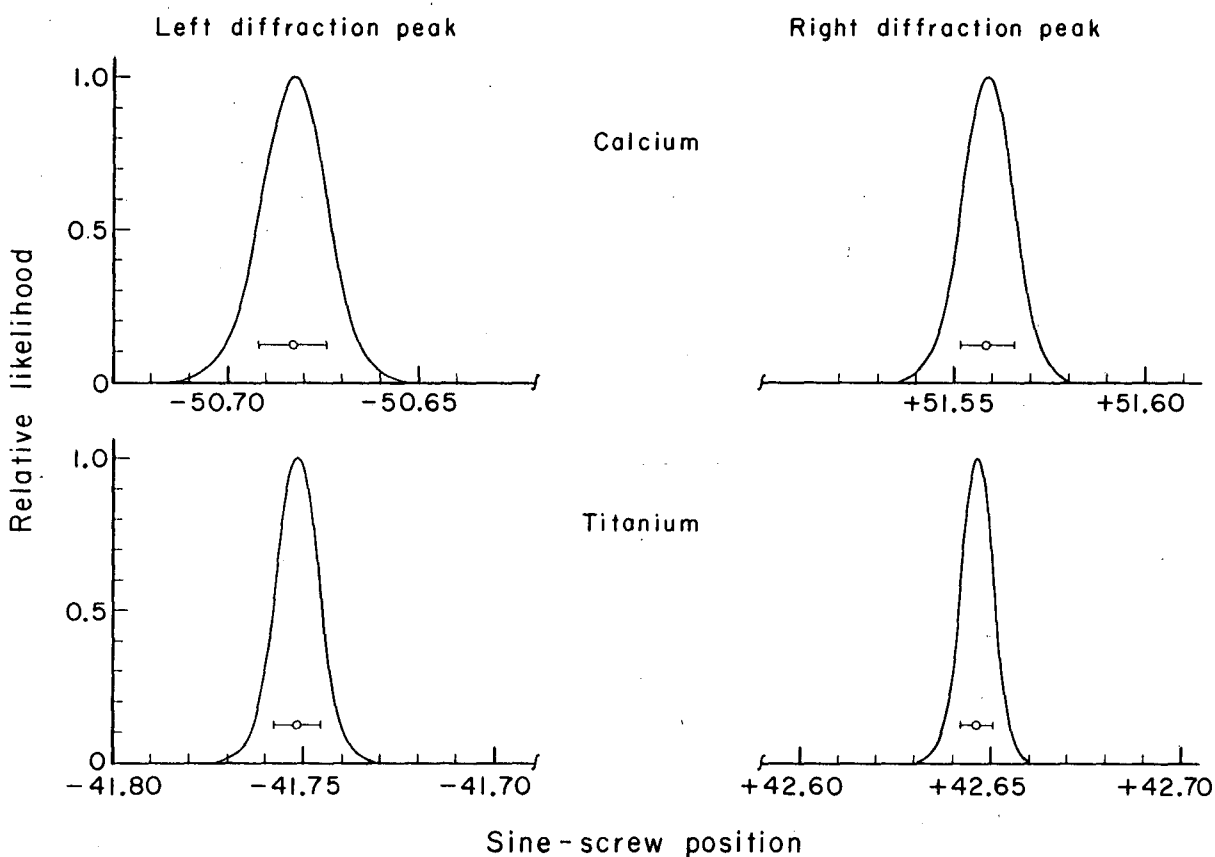
Fig. 21: The χ^2 for a diffraction peak least-squares fitted to the "Real" data, as a function of the diffraction peak location. The expected value of χ^2 is indicated.
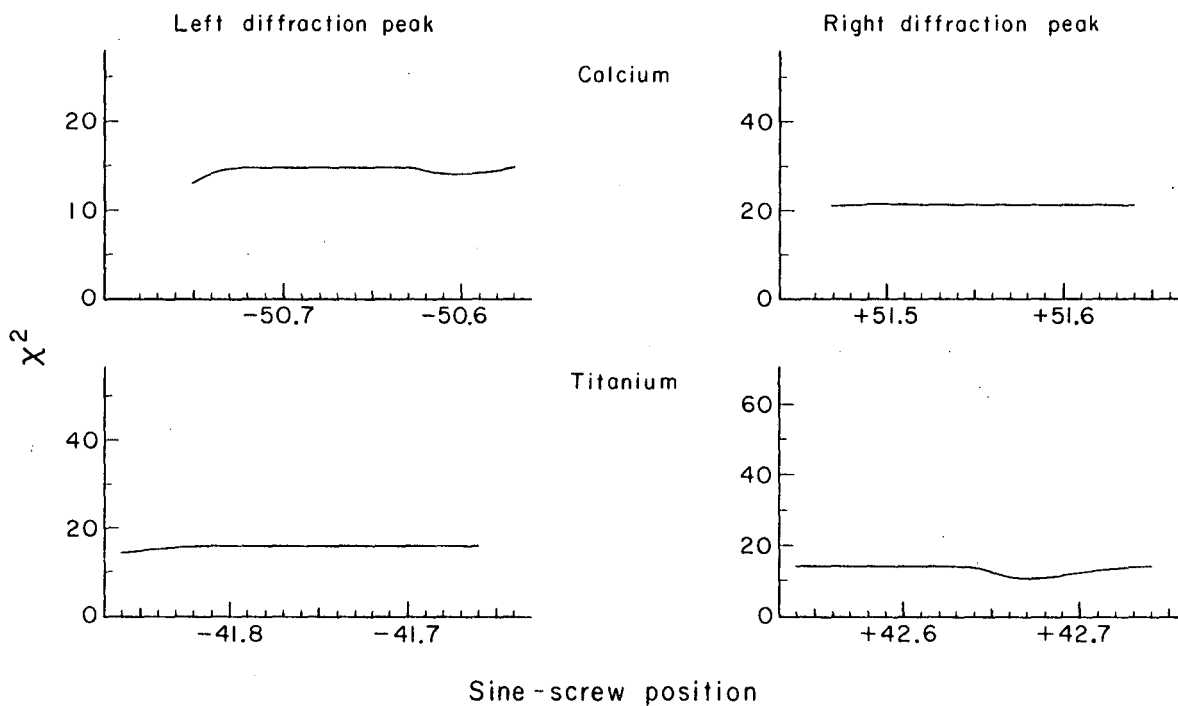
Fig. 22: The χ^2 for a diffraction peak least-squares fitted to the "Random" data, as a function of the diffraction peak location.

Fig. 23: The likelihood functions for the means of the diffraction
peaks in the "Real" data, derived directly from Figure 21. The
horizontal error flags represent the assigned means and standard
deviations.

are also indicated in Figure 19. The smooth curves in Figure 19 correspond to the maximum-likelihood distributions. Similarly, the smooth curves in Figure 20 correspond to the χ^2 minima in Figure 22.

The maximum-likelihood estimates of the background level in the four titanium curves (Figure 19 and 20) are self-consistent, as are the levels in the calcium data. In comparing the measured yields for titanium and the calculations in Section IVB, it is apparent that/expected signal-to-noise ratio was optimistic. It appears that an anomalously high background is the cause, although it could be due to an anomalously low yield if the ordinates in Figure 19 and 20 are inaccurate.

Based on the maximum-likelihood curves in Figure 19, and the total number of pions stopped for each measured point, the following information is obtained:

Parameter	Calcium Diffraction Peaks		Titanium Diffraction Peaks	
	Left	Right	Left	Right
"Signal" events in peak	176	199	341	375
Signal/noise ratio	0.58	0.77	0.80	1.23
"Signal" events rate at mode	2.3/hour	2.6/hour	2.3/hour	3.0/hour
Total running time	——— 320 hours ———		——— 360 hours ———	

The height of the two titanium diffraction peaks differ by almost two standard deviations. As the bent-crystal collimator alignment (see Figure 1) was checked both before and after the experiment and found to be satisfactory, the only explanation seems to be a statistical fluctuation ($\sim$ 5 per cent probability). Such a fluctuation is not expected to have any systematic effect on the location of the means of the diffraction peaks, however.

The experimental results are summarized in Table III.

Table III. Results of Experiment

Parameter	Calcium 4F-3D	Titanium 4F-3D
Diffraction peak location:		
Left (turns)	-50.6829 ± 0.0089	-41.7517 ± 0.0057
Right (turns)	+51.5585 ± 0.0068	+42.6462 ± 0.0042
Midpoint (turns)	+ 0.438 ± 0.006	+ 0.447 ± 0.004
Separation x 0.5 (turns)	51.1207 ± 0.0056	42.1989 ± 0.0036
$\sin \Theta_B$ (18°C)	0.0726120 ± 119 ppm	0.0599388 ± 84 ppm
Wavelength	171.004 xu ± 126 ppm	141.155 xu ± 98 ppm
Energy	72.352 keV ± 127 ppm	87.651 keV ± 99 ppm

The locations of the four diffraction peaks are the means and rms deviations of the four likelihood distributions in Figure 23.

The midpoints of each experiment (defined in Figure 12) differ by 1.1 standard deviations. Assuming the bent crystal alignment to be the same for both experiments, the probability of such a deviation occurring is about 20 per cent. (The other consistency check, of course, is the prediction of the pion mass by each x-ray measurement.)

The sine of the Bragg angles includes a correction for the average temperature deviation from $18^{\circ}C$. No correction to the estimated error is being included explicitly for the second moment of either the temperature correction or possible target motion, as both of these will affect the χ^2 directly by causing the measured distribution to deviate from the predicted shape.

The wavelengths and energies of the two pionic x-rays are based on the calibration of the quartz d spacing presented in Equation [2]. The fractional error for each energy measurement corresponds to $\pm$ 9 eV precision. This is to be compared to the $\pm$ 1 eV and $\pm$ 3 eV errors quoted on the two calibration lines.

VI.   CONCLUSIONS

A.   The Pion Mass

Combining the measured transition energies in Section IV E with the calculated scaling factors in Section III D yields the following estimates for the mass of the π^- meson:

Transition	π^- Mass
Calcium 4F-3D	139.582 ± 0.019 MeV
Titanium 4F-3D	139.574 ± 0.016 MeV

The weighted average of these two measurements is calculated in Appendix C,   yielding the final value for this experiment[81]

$$M_\pi c^2 = 139.577 \pm 0.014 \text{ MeV}$$

This estimate is in agreement with all of the precision measurements described in Section I. If the muon neutrino is assumed to be massless, the π^+ and π^- mass are found to be equal within 0.04 per cent. This is in agreement with the à priori assumption that the charged pion mass is invariant under CPT operation.

The effect of this measurement on the masses of the other mesons and hyperons is discussed by Barkas,[82] Rosenfeld et al.[83], and Schmidt.[84]

B.   The Muon Neutrino Mass Limit

As demonstrated by Barkas et al.[9], an upper limit on the muon neutrino mass may be assigned by applying energy-momentum conservation in $\pi \rightarrow \mu + \nu$ decay. For decay at rest $(c = 1 \text{ units})$

$$M_\nu^2 = (M_\pi - M_\mu)^2 - 2M_\pi T_\mu \qquad [13]$$

where T_μ is the kinetic energy of the recoil muon. The best present values for the input parameters are:

$$M_\pi = 139.577 \pm 0.014 \text{ MeV (this experiment)}$$

$$M_\mu = 105.659 \pm 0.002 \text{ MeV (Feinberg and Lederman)}[10]$$

$$P_\mu = 29.80 \pm 0.06 \text{ MeV (Barkas et al.)}[9]$$

The latter two combine to yield $T_\mu = 4.122 \pm 0.016$ MeV. The standard deviations of the first and second terms on the right-hand side of Equation 13 are due almost entirely to M_π and T_μ respectively, and therefore the two errors are essentially uncorrelated. A graphical solution of Equation 13 is illustrated in Figure 24. The bivariate Normal distribution may be projected onto the M_ν^2 axis yielding a qualitative upper limit of 2.1 MeV for the muon neutrino mass.

Literal interpretation of the figure, however, would yield only a 48 per cent probability that the neutrino mass is real, and a 52 per cent probability that it is imaginary. The imaginary root was introduced by the quadratic nature of the relation $E_\nu^2 = P_\nu^2 + M_\nu^2$, and may be removed by the condition $M_\nu \geqslant 0$. The Normal probability distribution for M_ν^2 is therefore truncated at $M_\nu^2 = 0$, and renormalized such that the probability of finding the neutrino mass in the interval $0 < M_\nu^2 < \infty$ is 100 per cent.

Analysis of the truncated distribution yields

$$0 < M_\nu < 2.1 \text{ MeV} \qquad 68 \text{ per cent probability}$$

$$0 < M_\nu < 2.7 \text{ MeV} \qquad 90 \text{ per cent probability}$$

The 2.1 MeV upper limit thus obtained is to be compared with the other estimates discussed in Section I.

Referring again to Figure 24, it is apparent that improvements in the estimates of the pion and muon masses will not significantly modify the present limit on the muon neutrino mass, but that a new precise measurement of T_μ (or P_μ) could reduce the upper limit to about 1 MeV.
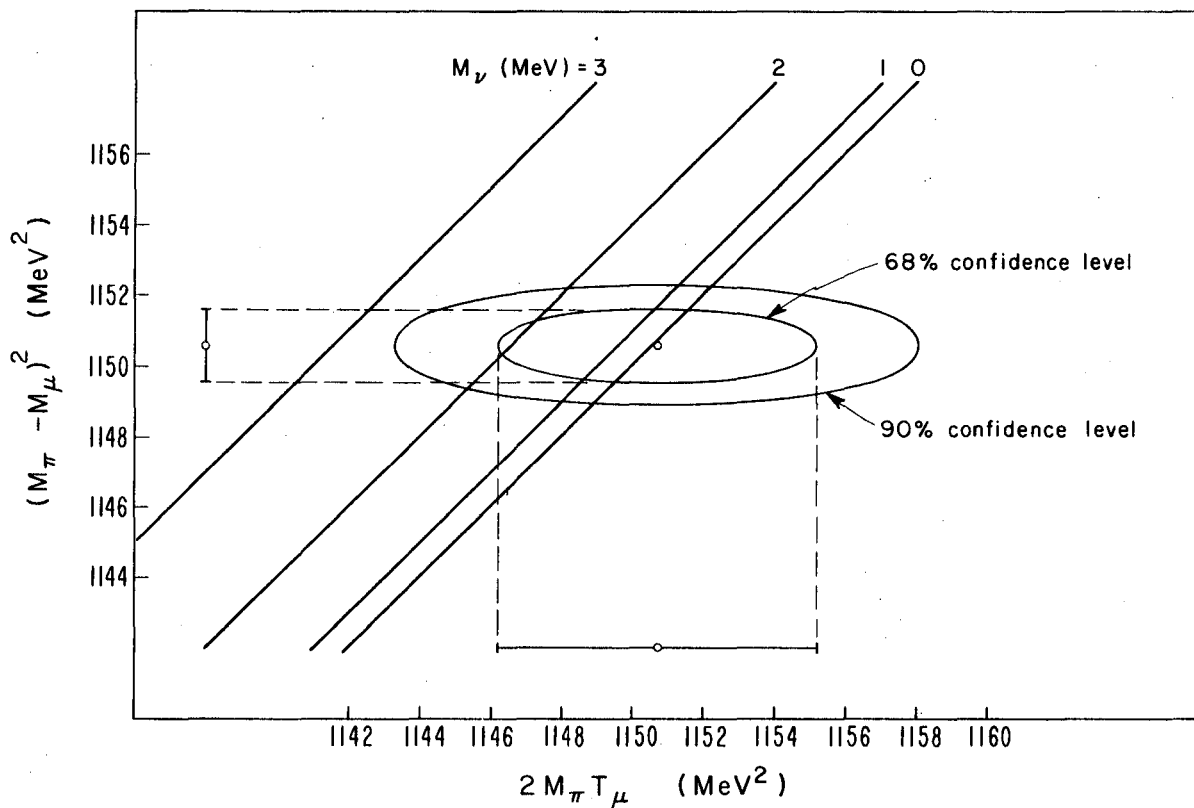
MUB-8510

Fig. 24: Graphical solution to Equation (13), using the current best estimates of M_π, M_μ, and T_μ (c = 1 units). All projections of the bivariate distribution are normal. As the standard deviations on the ordinate and abscissa are essentially uncorrelated, the error ellipses are not skewed. Projection onto the M_ν^2 axis yields a qualitative upper limit of 2.1 MeV for M_ν.

VI. ACKNOWLEDGEMENTS

VII APPENDICES

A. Localizing the Mean of a Gaussian Resolution Function

Often an experiment involves sampling counting rates over a resolution function in order to estimate the population mean. In planning experiments it is often worthwhile to make preliminary estimates of the variance of the sample mean about the population mean, once the resolution function, the signal-to-noise ratio, and the "signal" accumulation rate are known. Furthermore, it is often possible to adjust parameters of an experiment to maximize the rate of "information" accumulation of the population mean if the relationship between the other parameters is known.

The formalism of the derivation used here is similar to a calculation by DuMond,[19] but the resolution function and the method of presentation of results are quite different.

Let

$$y(x) = B + H \exp\left[\frac{-(x-x_o)^2}{2\sigma^2} \right] \qquad [A-1]$$

represent the average counting rate as a function of the variable x, where H/B represents the signal-to-noise ratio, and σ^2 the variance of the population, in this case a Gaussian distribution. The objective is to estimate σ_m^2, the variance of the sample mean about the population mean. Suppose the distribution $y(x)$ is scanned uniformly (as in a pulse-height analyzer for example) for a time t such that the number of events per unit (pulse-height) interval is on the average:

$$t \cdot y(x) = t\{B + H \exp[\frac{-(x-x_o)^2}{2\sigma^2}]\} \qquad [A-2]$$

The standard error on $t \cdot y(x)$ is then $[t \cdot y(x)]^{1/2}$. The corresponding

errors on the x and y coordinates are related by slope of $t \cdot y(x)$ (this

is discussed in statistics textbooks under the topic of linear regression).

This unit interval then contributes to the variance of the sample mean

an amount

$$\sigma_m(x) = [t \cdot y(x)]^{1/2} / t \cdot y'(x)$$

$$= \frac{\sigma^2}{\sqrt{tH}} \frac{\{B/H + \exp [\frac{-(x-x_o)^2}{2\sigma^2}]\}^{1/2}}{|x-x_o| \exp [\frac{-(x-x_o)^2}{2\sigma^2}]} \qquad [A-3]$$

The estimate of the variance of the sample mean about the population

mean is then:

$$\frac{1}{\sigma_m^2} = \int_{-\infty}^{\infty} \frac{dx}{\sigma_m^2(x)} = \frac{2\sqrt{2} \, tH}{\sigma} \int_{-\infty}^{\infty} \frac{x^2 \, e^{-2x^2}}{(B/H) + e^{-x^2}} \, dx \qquad [A-4]$$

the total number of "signal" events in the peak (not including back-

ground) is:

$$N = \int_{-\infty}^{\infty} t \, H \, \exp [\frac{-(x-x_o)^2}{2\sigma^2}] \, dx = t \, H \, \sigma \sqrt{2\pi} \qquad [A-5]$$

Thus the ratio of the variances is:

$$\frac{\sigma^2}{\sigma_m^2} = N \cdot f \, (H/B) \qquad [A-6]$$

where

$$f(H/B) = \frac{2}{\sqrt{\pi}} \int_{-\infty}^{\infty} \frac{x^2 \, e^{-2x^2}}{(B/H) + e^{-x^2}} \, dx$$

The function $f(H/B)$ is plotted in Figure 25. For the special case where

$B \rightarrow 0$ the ratio of variances becomes N as expected. As the rate of

accumulation of "information" is $(N/t) \cdot f(H/B)$ where (N/t) is the

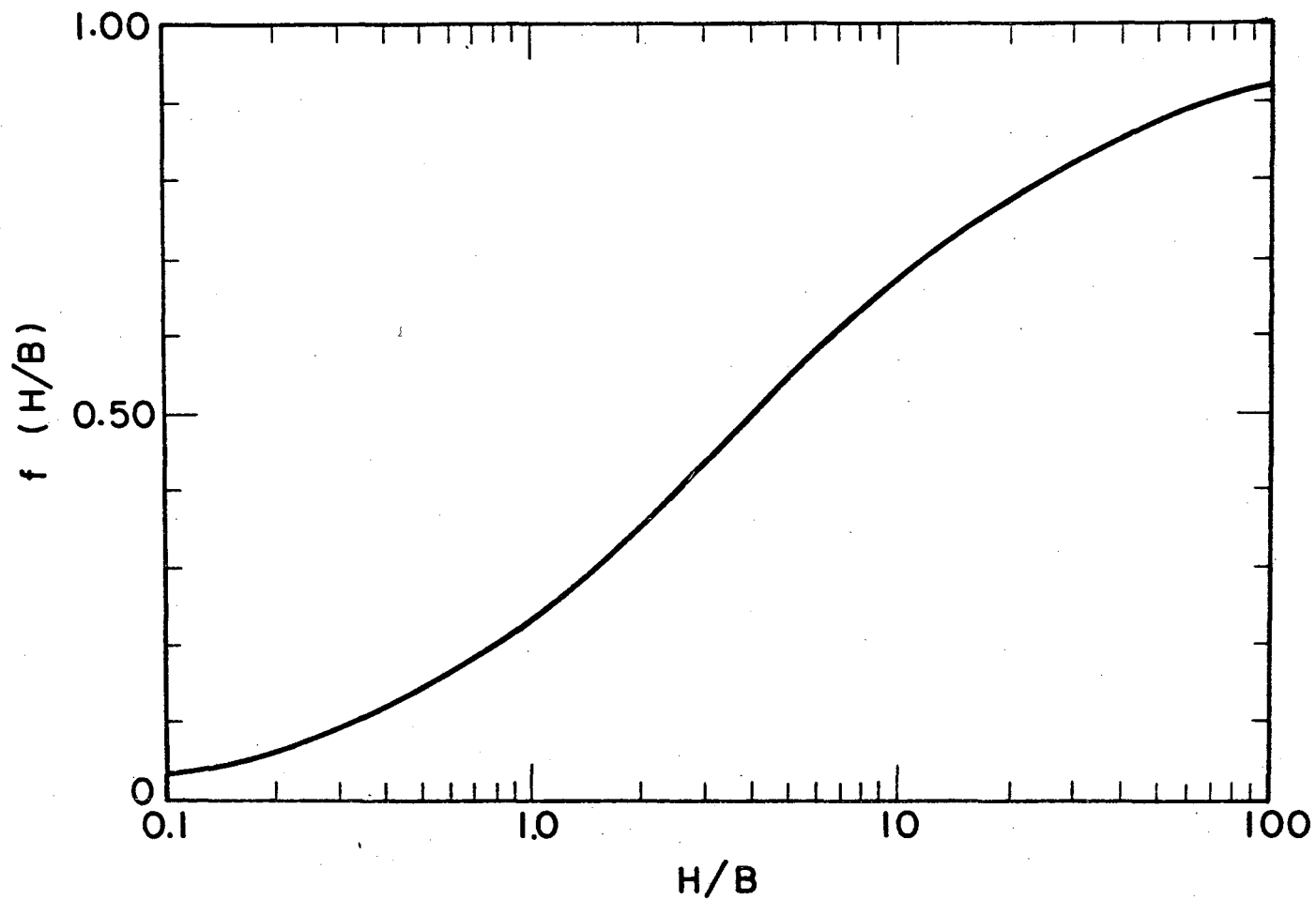"signal" accumulation rate, the function $f(H/B)$ may be referred to as

MU-36801

Fig. 25: Graphical evaluation of f(H/B) as defined in Equation (A-6) plotted
vs the signal-to-noise ratio H/B.

the "efficiency". Note for example that the "efficiency" for a signal-to-noise ratio of 1 is about 23 per cent of the ideal case (no background).

B. Vacuum Polarization Shift Using Relativistic Wave Functions

The relativistic radial wave equation for a spinless particle in a central Coulomb field is (from Section 42 of Schiff):[65]

$$\frac{1}{\rho^2} \frac{d}{d\rho} \left(\rho^2 \frac{dR}{d\rho} \right) + \left(\frac{\lambda}{\rho} - \frac{1}{4} - \frac{\ell(\ell+1) - \gamma^2}{\rho^2} \right) R = 0 \qquad \text{[A-7]}$$

where

$$\gamma = \alpha Z$$

$$\lambda = n - \ell - 1/2 + [(\ell + 1/2)^2 - \gamma^2]^{1/2}$$

$$\rho = 2(kr)$$

$$k = \frac{1}{\hbar c} [(M_\pi c^2)^2 - E^2]^{1/2} \; ; \; E = \text{total energy}$$

Substituting $R(\rho) = \rho^s e^{-\rho/2} u(\rho)$

where $s = \lambda - (n - \ell)$

$$\rho u'' + [2(s + 1) - \rho]u' - [s + 1 - \lambda] u = 0 \qquad \text{[A-8]}$$

Making the substitutions $b = 2(s + 1)$ and $a = s + 1 - \lambda$:

$$\rho u'' + (b - \rho) u' - au = 0$$

The solution is the confluent hypergeometric function as described in Section 20 of Schiff.[65] In the case of circular orbits $\ell = n - 1$, hence $s = \lambda - 1$ and $a = 0$. The normalized solution which is regular at $r = 0$ is then:

$$R(r) = \left[\frac{8 k^3}{\Gamma(2\lambda + 1)} \right]^{1/2} (2kr)^{\lambda-1} e^{-kr} \qquad \text{[A-9]}$$

In the non-relativistic limit this reduces to the hydrogen-atom radial wave functions.

The second order vacuum polarization shift by first-order perturbation theory is:

$$\Delta E = -e < R \mid \Delta \varphi \mid R >$$
$$= -Ze^2 < R \mid \frac{1}{r} (\frac{\Delta \varphi}{\varphi_c}) \mid R > \qquad [A-10]$$

where

$$(\frac{\Delta \varphi}{\varphi_c}) = (\frac{\alpha}{3\pi}) \int_1^\infty \frac{e^{-2\mu r x} \sqrt{x^2-1} (2x^2+1)}{x^4} \, dx$$

is the Uehling integral[68] where $\mu = mc/\hbar$ is the inverse electron Compton wavelength. The integration over r may be performed, yielding,

$$\Delta E = -(\frac{\alpha}{3\pi}) \frac{Ze^2 k}{\lambda} \int_1^\infty \frac{\sqrt{x^2-1}(2x^2+1)}{x^4 (1 + \frac{\mu x}{k})^{2\lambda}} \, dx \qquad [A-11]$$

which reduces to the expression derived by Mickelwait[70] and Koslov[71] in the non-relativistic limit.

The substitution $x = 1/v$ yields

$$\Delta E = -(\frac{\alpha}{3\pi}) \frac{Ze^2 k}{\lambda} \int_0^1 \frac{\sqrt{1-v^2} (2+v^2) v^{2\lambda-1}}{(v + \frac{\mu}{k})^{2\lambda}} \, dv \qquad [A-12]$$

which is more suitable for computer evaluation.

In particular, for the 4F-3D transitions in pionic calcium and titanium (using a reduced mass derived from $M_\pi c^2 = 139.58$ MeV):

Energy Level	Vacuum Polarization Shift	
	Relativistic	Non-Relativistic
Calcium 3D	-316.4 eV	-315.1 eV
Calcium 4F	- 87.4	- 87.2
Titanium 3D	-420.1	-418.1
Titanium 4F	-120.4	-120.0

C. Error Analysis

The calcium and titanium measurements each predict a maximum likelihood value of the π^- mass with an associated error. In forming the weighted average of these measurements, it is necessary to include consideration of error correlations. Glasser[86] shows that in general,

$$\overline{X} = \sum_i k_i X_i \qquad \text{where } k_i = \frac{\sum_j G_{ij}^{-1}}{\sum_{ij} G_{ij}^{-1}} \qquad \text{[A-13]}$$

with a variance

$$\sigma^2(\overline{X}) = \frac{1}{\sum_{ij} G_{ij}^{-1}} \quad \text{where G is the error matrix,}$$

is the/weighted average with minimum variance.

The predicted values of the π^- mass are:

Calcium   139.582 MeV

Titanium   139.574 MeV

The contributions to the errors in these measurements are (r_{12} is the correlation coefficient):

Source of Error	Calcium	Titanium	r_{12}
Counting Statistics	119 ppm	84 ppm	0
Calibration Error	42	51	+1
Energy Level Calculation	55	57	+1
Wavelength-energy Conversion	15	15	+1

Therefore:

$$G = \begin{pmatrix} 1.42 & 0 \\ 0 & 0.71 \end{pmatrix} + \begin{pmatrix} 0.18 & 0.21 \\ 0.21 & 0.26 \end{pmatrix} + \begin{pmatrix} 0.30 & 0.31 \\ 0.31 & 0.32 \end{pmatrix} + \begin{pmatrix} 0.02 & 0.02 \\ 0.02 & 0.02 \end{pmatrix} = \begin{pmatrix} 1.92 & 0.54 \\ 0.54 & 1.31 \end{pmatrix}$$

where G_{ij} is in units of $(100 \text{ ppm})^2$ and

$$G_{11} = \text{variance of calcium measurement}$$

$$G_{22} = \text{variance of titanium measurement}$$

$$G^{-1} = \frac{1}{2.23} \begin{pmatrix} 1.31 & -0.54 \\ -0.54 & 1.92 \end{pmatrix} = \begin{pmatrix} 0.59 & -0.24 \\ -0.24 & 0.86 \end{pmatrix}$$

hence $k_1 = 0.36$, $k_2 = 0.64$ and $\sigma^2(\overline{X}) = (101 \text{ ppm})^2$

The results are:

Calcium measurement	139.582 ± 0.019 MeV
Titanium measurement	139.574 ± 0.016 MeV
Weighted average	139.577 ± 0.014 MeV

FOOTNOTES AND REFERENCES

1. J. A. Wheeler and R. Ladenburg, Phys. Rev. $\underline{60}$, 754 (1941).

2. C. F. Powell, Rept. Progr. Phys. $\underline{13}$, 350 (1950).

3. E. R. Cohen, K. M. Crowe, and J. W. M. DuMond, Phys. Rev. $\underline{104}$, 266 (L) (1956); and Fundamental Constants of Physics. (Inter-science Publishers Inc., New York, 1957).

4. K. M. Crowe, Nuovo Cimento (10) $\underline{5}$, 541 (1957).

5. M. Stearns, M. B. Stearns, S. DeBenedetti, and L. Leipuner, Phys. Rev. $\underline{95}$, 1353 (L) (1954).

6. K. M. Crowe and R. H. Phillips, Phys. Rev. $\underline{96}$, 470 (1954)[a].

7. The abbreviation "fwhm" for full width at half maximum will be used throughout this paper.

8. J. B. Czirr, Phys. Rev. $\underline{130}$, 341 (1963).

9. G. Bingham, private communication, 1965 (unpublished).

10. W. H. Barkas, W. Birnbaum, and F. M. Smith, Phys. Rev. $\underline{101}$, 778 (1956).[a]

11. G. Feinberg and L. M. Lederman, Ann. Rev. Nucl. Sci. $\underline{13}$, 431 (1963).

12. W. F. Dudziak, R. Sagane, and J. Vedder, Phys. Rev. $\underline{114}$, 336 (1959).

13. M. Bardon, P. Norton, J. Peoples, A. M. Sachs, and J. Lee-Franzini, Phys. Rev. Letters $\underline{14}$, 449 (1965).

14. H. P. Stapp, Nuovo Cimento (10) $\underline{32}$, 103 (1964).

15. J. A. Bearden, X-Ray Wavelengths (U.S.A.E.C. Report No. NYO-10586, 1964) (unpublished).[a] This is a 530 page compilation of measurements of the wavelengths of more than 25,000 electronic x-rays.

16. J. W. M. DuMond and H. A. Kirkpatrick, Rev. Sci. Instr. $\underline{1}$, 88 (1930).

17. J. W. M. DuMond, Rev. Sci. Instr. $\underline{18}$, 626 (1947).

18. J. W. M. DuMond, in Beta and Gamma Ray Spectroscopy (edited by K. Sieghahn, North Holland Pub. Co., Amsterdam, 1955), p. 100.

19. J. W. M. DuMond, Ergeb. Exakt. Naturw. $\underline{28}$, 232 (1955).

20. J. W. M. DuMond, Ann. Rev. Nucl. Sci. $\underline{8}$, 163 (1958).

21. G. A. Bartholomew, J. W. Knowles, and G. E. Lee - Whiting, Rept. Progr. Phys. $\underline{23}$, 453 (1960).

22. J. W. Knowles, in Beta and Gamma Ray Spectroscopy (edited by K. Seigbahn, North Holland Publishing Co., Amsterdam, 1965) p. 203.

23. D. Rose, H. Ostrander, and B. Hamermesh, Rev. Sci. Instr. 28, 233 (1957). For a more complete description see Argonne National Laboratory report ANL 5642, December 1956. (Unpublished).

24. E. J. Seppi, H. Hendrickson, F. Boehm, and J. W. M. DuMond, Nucl. Instr. and Meth. 16, 17 (1962).

25. Engraved by W. and L. E. Gurley, Troy, New York.

26. H. Ostrander, American Machinist 100, 118 (July 2, 1965).

27. Bor-Al is a trademark of Brooks and Perkins Inc. Detroit Mich. The plate is a sandwich of boron carbide between two layers of aluminum, is 35 per cent natural boron by weight.

28. An excellent description of the Hartmann test is given by Ref. 19, pages 267-268.

29. D. A. Lind, W. J. West, and J. W. M. DuMond, Phys. Rev. 77, 475 (1950).

30. W. H. Zachariasen, Theory of X-Ray Diffraction in Crystals (John Wiley and Sons, Inc. New York, 1945).

31. I. Marklund and B. Lindstrom, Nucl. Phys. 40, 329 (1963), measure an energy of 84.260 ± 0.004 keV for this transition (their quoted value has been modified slightly from 84.262 ± 0.004 keV due to a re-evaluation of the wavelength of their calibration line).[15] F. Boehm and C. Gunther (private communication, 1965) have measured this line by direct comparison with the K_α x-rays[15], yielding the value 84.261 ± 0.003 keV.

32. B. B. Watson, W. J. West, D. A. Lind, and J. W. M. DuMond, Phys. Rev. 75, 505 (1949).

33. S. DeBenedetti, Nuovo Cimento (10) 4, 1209 (1956).

34. M. B. Stearns, Progr. Nucl. Phys. 6, 108 (1957). (annual)

35. D. West, Rept. Progr. Phys. 21, 271 (1958).

36. A. Petermann and Y. Yamaguchi, Phys. Rev. Letters 2, 359 (1959).

37. R. P. Feynman, in Solvay Institute, 12th Physics Conference Proceedings (Interscience, New York, 1961) p. 61.

38. M. B. Stearns, M. Stearns, L. Leipuner, and S. DeBenedetti, Phys. Rev. 95, 625A (1954).

39. S. Deser, M. L. Goldberger, K. Baumann, and W. Thirring, Phys. Rev. 96, 774 (1954).

40. H. A. Bethe and F. De Hoffmann, *Mesons and Fields*, Vol. II (Row Peterson and Co., White Plains, N. Y., 1955) p. 103.

41. K. A. Brueckner, Phys. Rev. 98, 769 (1955).

42. R. Karplus, Proceedings of the 1956 Rochester Conference (Interscience, New York, 1956) p. IX-33.

43. R. Karplus and F. Halpern, Bull. Am. Phys. Soc. (2) 2, 5 (1957).

44. M. Camac, A. D. M. McGuire, J. B. Platt, and H. J. Schulte, Phys. Rev. 99, 897 (1955).

45. M. Stearns and M. B. Stearns, Phys. Rev. 103, 1534 (1956).

46. D. West and E. F. Bradley, Phil. Mag. (8) 2, 957 (1957).

47. N. Byers, Phys. Rev. 107, 843 (1957).

48. A. I. Lebedev, J.E.T.P. 8, 729 (1958).

49. T. L. Trueman, Nucl. Phys. 26, 57 (1961).

50. Y. Eisenberg and D. Kessler, Phys. Rev. 130, 2352 (1963).

51. L. Wolfenstein, Equation 13 in Reference 45. Also, Bull. Am. Phys. Soc. (2) 2, 39 (1957).

52. L. S. Kisslinger, Phys. Rev. 98, 761 (1955).

53. W. F. Baker, H. Byfield, and J. Rainwater, Phys. Rev. 112, 1773 (1958).

54. T. E. O. Ericson, CERN Report 63-28 (1963)(unpublished).

55. M. Ericson, Compt. Rend. 257, 3831 (1963).

56. M. Ericson and T. E. O. Ericson, Compt. Rend. Congr. Intern. Phys. Nucl. 2, 232 (1964).

57. M. Ericson and T. E. O. Ericson, (1965), to be published in Annals of Physics (unpublished).

58. A. Astbury, J. P. Deutsch, K. M. Crowe, R. E. Shafer, and R. E. Taylor, Compt. Rend. Congr. Intern. Phys. Nucl. 2, 225 (1964). See also, Bull. Am. Phys. Soc. (2) 9, 393 (1964).

59. D. A. Jenkins, private communications, 1965 (unpublished) and Bull. Am. Phys. Soc. (2) 10, 1123 (1965).

60. T. Mottershead, private communication, 1965 (unpublished).

61. This estimate is in agreement with an estimate by M. Ericson and

T. E. O. Ericson, private communication, 1965 (unpublished).

62. Y. Eisenberg and D. Kessler, Phys. Rev. 123, 1472 (1961).

63. M. A. Ruderman, Phys. Rev. 118, 1632 (1960).

64. M. Stearns, M. B. Stearns, G. Culligan, B. Sherwood, and V. L. Telegdi, Bull. Am. Phys. Soc. (2), 9, 81 (1964).

65. L. I. Schiff, Quantum Mechanics (McGraw Hill Book Co., 1949).

66. E. R. Cohen and J. W. M. DuMond, Rev. Mod. Phys. 37, 537 (1965).

67. G. Breit and G. E. Brown, Phys. Rev. 74, 1278 (1948).

68. E. A. Uehling, Phys. Rev. 48, 55 (1935).

69. L. Foldy and E. Eriksen, Phys. Rev. 95, 1048 (1954).

70. A. B. Michelwait, thesis, Carnegie Institute of Technology, 1954 (unpublished); A. B. Mickelwait and H. C. Corben, Phys. Rev. 96, 1145(1954).

71. S. Koslov, Nevis Cyclotron Laboratory Report No. 19, 1956 (unpublished).

72. E. Wichmann and N. Kroll, Phys. Rev. 101, 843 (1956).

73. R. Glauber, W. Rarita, and P. Schwed, Phys. Rev. 120, 609 (1960).

74. M. Baranger, F. Dyson, and E. Salpeter, Phys. Rev. 88, 680 (1952).

75. E. U. Condon and G. H. Shortley, Theory of Atomic Spectra (Cambridge University Press, 1951) p. 136.

76. The alignment telescope was a Keuffel and Esser Model 71-2022 with an angular magnification of 47 X and a resolving power of 3.4 seconds of arc.

77. L. G. Hyman, Rev. Sci. Instr. 36, 193 (1965).

78. R. F. Post and L. I. Schiff, Phys. Rev. 80, 1113 (L) (1950).

79. Radiation Laboratory Counting Handbook, UCRL - 3307 (revised) (Edited by Nuclear Instrumentation Groups, 1964) (unpublished).

80. R. T. Birge, Phys. Rev. 40, 207 (1932).

81. A preliminary estimate of $M_\pi c^2 = 139.580 \pm 0.015$ MeV, based on this experiment, has been presented by R. E. Shafer, K. M. Crowe, and D. A. Jenkins, Phys. Rev. Letters 14, 923 (1965).

82. W. H. Barkas, Ann. Rev. Nucl. Sci. 15, 67 (1965).

83. A. H. Rosenfeld, A. Barbaro-Galtieri, W. H. Barkas, P. L. Bastien, J. Kirz, and M. Roos, Rev. Mod. Phys. 37, 633 (1965).

84. P. Schmidt, Phys. Rev. 140, B1328 (1965).

85. R. G. Glasser, U. S. Naval Research Laboratory Report No. NRL 5667, (1961) p. 34 (unpublished).

[a]These authors have chosen to express their errors in units other than standard deviations. Assuming a Normal error curve, their deviations have been re-expressed as a standard error in this paper.